Citation (APA)
Jangda, Z., Bultreys, T., Jiang, Z., Foroughi, S., Menke, H., Busch, A., Geiger, S., & Singh, K. (2026). Pore-scale analysis of hydrogen-water displacement in sandstones: a comparison of pore-network modelling and flow visualisation experiments. *International Journal of Multiphase Flow*, *201*, Article 105776. https://doi.org/10.1016/j.ijmultiphaseflow.2026.105776

International Journal of Multiphase Flow 201 (2026) 105776

Contents lists available at ScienceDirect

International Journal of Multiphase Flow

journal homepage: www.elsevier.com/locate/ijmulflow

Research Paper

Pore-scale analysis of hydrogen-water displacement in sandstones: a comparison of pore-network modelling and flow visualisation experiments

Zaid Jangda [a,b,*], Tom Bultreys [c], Zeyun Jiang [a], Sajjad Foroughi [d], Hannah Menke [a], Andreas Busch [b], Sebastian Geiger [e], Kamaljit Singh [a]

[a] Institute of GeoEnergy Engineering, Heriot-Watt University, UK
[b] The Lyell Centre, Heriot-Watt University, UK
[c] PProGRess, Department of Geology, Ghent University, Belgium
[d] Department of Earth Science and Engineering, Imperial College London, UK
[e] Department of Geoscience and Engineering, Delft University of Technology, The Netherlands

HIGHLIGHTS

- Quasi-static pore-network model can represent hydrogen-water displacement in homogeneous sandstones.
- Layered heterogeneity limits model performance in predicting trapping and fluid redistribution.
- Pore-scale imaging provides a benchmark for evaluating multiphase flow models.

GRAPHICAL ABSTRACT

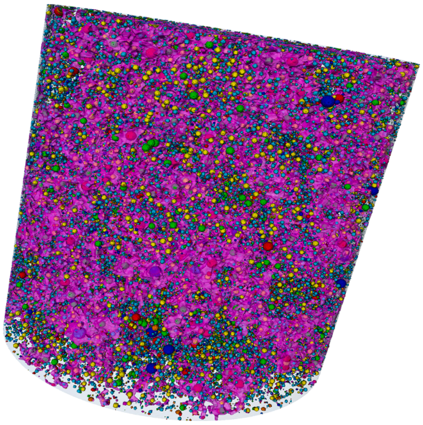

ARTICLE INFO

Keywords:
Pore-network modelling
Gas-liquid displacement
Multiphase flow in porous media
Pore-scale imaging

ABSTRACT

Hydrogen–water displacement in porous rocks involves capillary-dominated multiphase-flow processes at the pore scale that are critical for understanding fluid distribution, trapping, and recovery behaviour. Three-dimensional pore-scale flow visualisation experiments provide direct insight into these processes but are resource intensive and technically challenging. Pore-network models offer a computationally efficient alternative for simulating capillary-dominated multiphase flow, but their accuracy depends on how well-simplified displacement rules represent real pore-scale behaviour.

This work presents a direct pore-by-pore comparison between experimentally observed displacement events and predictions from a quasi-static pore-network model. The comparison enables evaluation of the model's simplifying assumptions and its ability to reproduce pore-scale displacement behaviour across contrasting rock types, including a homogeneous Bentheimer sandstone and a layered Clashach sandstone. The model was

---

* Corresponding author.
E-mail address: zaid.jangda@hw.ac.uk (Z. Jangda).

https://doi.org/10.1016/j.ijmultiphaseflow.2026.105776
Received 21 January 2026; Received in revised form 4 May 2026; Accepted 19 May 2026

calibrated to match experimental end-state saturations, and its performance was evaluated using spatial saturation distributions and pore-occupancy statistics.

The pore-network model shows good agreement with experimental observations for the homogeneous rock, particularly during drainage. It is subsequently used to analyse additional scenarios, including cyclic hydrogen injection and withdrawal and wettability variations, providing insight into capillary pressure behaviour and residual saturation trends. In contrast, for the heterogeneous rock, the model does not fully capture the trapping and fluid redistribution observed experimentally, indicating limitations in representing fine-scale heterogeneity.

Overall, the results identify the conditions under which the quasi-static pore-network model can reliably represent hydrogen–water displacement and where its simplifying assumptions become limiting, providing guidance for its application in pore-scale multiphase-flow research.

1. Introduction

Subsurface porous formations offer a promising solution for storing large volumes of hydrogen (H_2), which is essential for the rapid transition to cleaner energy and for balancing supply and demand in renewable energy systems (Heinemann et al., 2021; Krevor et al., 2023; Miocic et al., 2022; Muhammed et al., 2022). Understanding the pore-scale flow and trapping behaviour of H_2 within these geological formations is crucial for assessing storage capacity and recovery efficiency (Tarkowski, 2019; Zivar et al., 2021).

Large-scale reservoir models require constitutive relationships such as capillary pressure (P_c) and relative permeability (k_r) curves, which depend on factors such as interfacial tension, contact angle, and pore-space morphology (Armstrong et al., 2016a; Bultreys et al., 2018). Pore-scale studies provide these inputs through either experimental methods or numerical modelling of multiphase fluid flow (Blunt, 2016). While direct experimental visualisation of H_2 flow in rocks provides invaluable insights for large-scale reservoir models, it remains technically challenging and resource intensive (Goodarzi et al., 2024; Thaysen et al., 2023).

Numerical methods such as lattice-Boltzmann (Alpak et al., 2018; Ramstad et al., 2012; Wang et al., 2024) and finite-volume Navier--Stokes solvers (Raeini et al., 2014) calculate flow and pressure fields directly on three-dimensional (3D) images of the pore space, providing accurate pore-scale simulations. These simulations can resolve interface dynamics and capillary phenomena in detail, but are computationally intensive and typically constrained to small domains. For complex and heterogeneous rocks, adequately resolving the representative elementary volume requires large image sizes, significantly increasing computational cost and limiting the feasibility of scenario testing or sensitivity analysis (Armstrong et al., 2016a; Ellman et al., 2024; Maes et al., 2021; Patsoukis Dimou et al., 2021; Ruspini et al., 2021).

Pore-network models (PNMs) provide a computationally efficient tool for simulating multiphase flow in porous media by representing pore-spaces as networks of interconnected pores and throats with idealized geometries (Bultreys et al., 2018; Hashemi et al., 2021a; Petrovskyy et al., 2021). These geometries enable rapid calculation of key flow properties such as capillary entry pressure, hydraulic conductance, and phase saturation (Øren et al., 1998; Ruspini et al., 2021). Typically, PNMs designed to simulate multiphase flow in rocks assume quasi-static pore-scale physics, where fluid displacement is governed by capillary forces under the assumption of capillary equilibrium. Viscous forces are neglected, making these models particularly suited to capillary-dominated flow regimes (Ruspini et al., 2021). The use of capillary displacement rules, grounded in experimental observations (Lenormand et al., 1983), aims to strike a balance between computational efficiency, physical interpretability, and modelling flexibility (Øren et al., 1998; Valvatne et al., 2004). These models have been extensively used for exploring flow behaviour across a broad range of conditions and for conducting parametric studies, including those involving wettability variation, cyclic injection, and pore-scale trapping dynamics (Bultreys et al., 2020; Foroughi et al., 2025; Mascini et al., 2020; Øren et al., 2019; Ryazanov et al., 2009; Zhao et al., 2019).

Studies have shown that quasi-static PNMs can reproduce experimental k_r curves in homogeneous or structurally simple rock samples (Blunt et al., 2013; Foroughi et al., 2025; Øren et al., 2003, 1998; Valvatne et al., 2004), and that their predictive capability improves when image-derived contact angles are incorporated (Foroughi et al., 2025). However, their application to H_2-water systems remains limited (Alaamri et al., 2023; Hashemi et al., 2021a; Wang et al., 2023a). Hydrogen presents unique challenges for pore-scale modelling due to its low viscosity and density, high mobility and compressibility, and its solubility in the aqueous phase (Heinemann et al., 2021). These properties increase the likelihood of dynamic flow effects, such as Haines jumps, Ostwald ripening, and intermittent displacement events, even under conditions where capillary forces are expected to dominate (Blunt, 2022; Goodarzi et al., 2024; Thaysen et al., 2025; Zhang et al., 2023). These effects can lead to local redistribution of the non-wetting phase. In heterogeneous systems, permeability contrasts and connectivity transitions may concentrate flow into preferential pathways, thereby amplifying such transient effects. These phenomena are inherently absent from quasi-static PNMs, which assume instantaneous pressure equilibrium and neglect viscous and inertial forces. Observations from micro-CT flow imaging experiments for oil-water and CO_2-water systems indicate that dynamic effects can still occur even at very low capillary numbers ($Ca < 10^{-6}$) (Armstrong et al., 2016a; Berg et al., 2013; Rücker et al., 2015; Schlüter et al., 2017; Singh et al., 2017; Wildenschild et al., 2013), thereby challenging the validity of the quasi-static assumption at these conditions. This raises an important question about the extent to which quasi-static pore-network models can reproduce pore-scale H_2-water displacement behaviour observed in pore-scale experiments.

Additionally, to the points raised above, the accuracy of pore-network model (PNM) predictions depend on the assumptions made during both pore-network extraction and flow simulation (Bondino et al., 2013; Liu et al., 2015). The abstracted geometry and simplified physics, while central to the model's computational efficiency (Wang et al., 2021), inherently limit its predictive capabilities (Sorbie et al., 2012). Various methods exist for generating networks from micro-Computed Tomography (micro-CT) images, including medial axis, grain-based, maximum ball, and watershed segmentation approaches (Bakke et al., 1997; Ellman et al., 2024; Lindquist et al., 1996; Wildenschild et al., 2013), each introducing geometric simplifications. However, the predictive performance of PNMs has significantly improved with the development of extraction algorithms that better preserve the essential geometrical and topological features of the pore space (Dong et al., 2009; Lindquist et al., 1999, 2000; Silin et al., 2006). Pore-network models simplify the complex physics of multiphase flow, making them useful to assess whether such simplifications yield reasonable or informative results. By identifying where these models succeed or fall short, PNMs can enhance our mechanistic understanding and help pinpoint which aspects of the flow processes warrant deeper investigation (Ellman et al., 2024). For multiphase systems, PNMs are generally reliable for modelling drainage but less so for imbibition, due to their limited capacity to simulate snap-off events and disconnected ganglia distributions (Ellman et al., 2024; Gostick et al., 2022; Helland et al., 2017).

In this study, we evaluate the ability of a widely employed quasi-static PNM to reproduce experimentally observed H_2-water displacement behaviour in sandstone rocks. We apply the model developed at Imperial College London (Bultreys et al., 2018; Hashemi et al., 2021a; Raeini et al., 2017; Valvatne et al., 2004) to simulate H_2 displacement in two different rock samples, a homogeneous Bentheimer and a layered Clashach sandstone. Simulations are matched against recent 3D pore-scale visualisation experiments on both rock types (Jangda et al., 2023, 2024a) to assess how well the model can reproduce observed saturation profiles and pore occupancy trends. For the homogeneous Bentheimer sandstone, where simulation and experiment show good agreement, the model is further extended to explore sensitivity to wettability and multiple injection and withdrawal cycles. These additional predictions, which are difficult to obtain experimentally, yield P_c curves under varying conditions, which are important input parameters for large-scale reservoir modelling.

By comparing experimental observations with PNM predictions, this study offers new insights into the applicability and limitations of PNMs for modelling H_2 flow in subsurface formations. These findings help to clarify the current capabilities of PNMs for underground hydrogen storage (UHS) and help define priorities for future development and integration with experimental studies. By identifying where the model succeeds and where it fails, we seek to clarify the conditions under which PNM-derived predictions can be meaningfully used to inform larger-scale flow descriptions.

2. Methodology

2.1. Experimental process

The H_2-water flow visualisation experiments were conducted using high-resolution X-ray micro-CT imaging to observe pore-scale fluid displacement in two different rock samples: a homogeneous Bentheimer sandstone and a heterogeneous layered Clashach sandstone. These experiments, including the imaging and segmentation workflows, have been reported previously in Jangda et al. (2023, 2024a) and the datasets are available via Jangda et al. (2022, 2024b). The Bentheimer sample has a relatively uniform pore size distribution, while the Clashach sample contains a thin layer of smaller pores and throats sandwiched between layers of comparatively larger pores and throats, as shown in Fig. 1, creating heterogeneity in the flow pathway. This layered configuration introduces permeability contrasts and preferential flow pathways that distinguish it from the relatively uniform pore structure of the Bentheimer sandstone. The Bentheimer sample is therefore considered structurally homogeneous at the scale of investigation, whereas the Clashach sample represents a layered heterogeneous system.

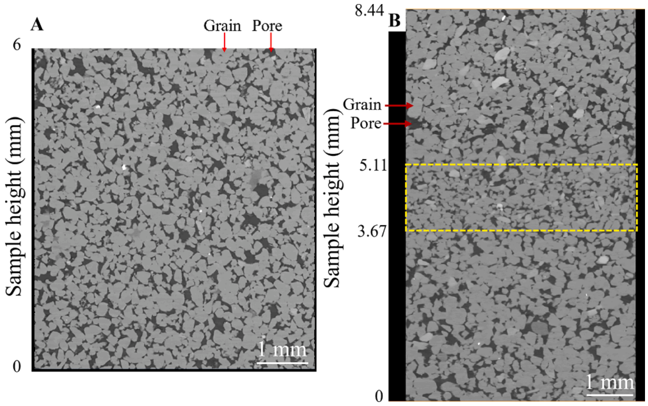

Fig. 1. 2D vertical cross sections of (A) the homogeneous Bentheimer and (B) the heterogeneous Clashach sandstone samples. In (B) the middle layer consisting of smaller pores and throats is highlighted within the yellow-dashed rectangle.

Core samples of 6 mm diameter were prepared from each rock type, with lengths of 27.0 mm for the Bentheimer and 12.4 mm for the Clashach sample. The core samples were placed inside a PEEK core holder mounted on a rotating stage within a micro-CT scanner and initially saturated with brine (4% KI-saturated water) that had been pre-equilibrated with H_2 in a high-pressure, high-temperature (HPHT) reactor at the experimental conditions of 50 °C and 100 bar. The core holder was subsequently maintained at these temperature and pressure settings to replicate subsurface reservoir conditions during the experiment. Hydrogen was then injected into the brine-filled samples from the top (drainage) to ascertain the initial H_2 storage capacity of the rock, followed by brine injection from the bottom to recover the H_2 (imbibition). Fluid injections were carried out under constant flow rates, maintained by high-precision syringe pumps, representing a capillary-dominated flow regime ($Ca < 10^{-6}$). The injection cycles lasted approximately 60 minutes for drainage and 20 minutes for imbibition, corresponding to the injection of 15 PV of H_2 during drainage and 5 PV of brine during imbibition.

The central section of each rock sample, corresponding to a length of 6.7 mm for the Bentheimer sample and 8.8 mm for the Clashach sample, was scanned using micro-CT before brine saturation to capture the dry state. The scans were repeated after drainage and imbibition to visualise and quantify fluid distributions, pore saturations, and pore occupancy. Imaging was performed immediately after completion of each injection stage. Each scan required approximately 2 hours, after which the subsequent fluid injection was immediately started. The images therefore represent the fluid configuration following each displacement step rather than instantaneous configurations during active flow. The resulting images were processed and segmented to distinguish between the rock, H_2, and brine phases. Fluid saturations and pore occupancy measurements were performed using Avizo software (Thermo Fisher Scientific), providing a detailed assessment of H_2 displacement and trapping in the pore-space. The experimental procedure and image analysis technique have been described in detail in our previous studies (Jangda et al., 2023, 2024a), and the data from these works serve as a benchmark for validating the PNM simulations.

2.2. Pore-network model simulations

A quasi-static PNM was used to simulate H_2 flow and trapping behaviour in the two rock types. The PNM simulation consists of two main steps:

2.2.1. Network extraction

The pore networks were extracted using an open-source code ('pn extract', Imperial College, London), which employs a watershed algorithm using maximum inscribed spheres clustering to find seed points, to extract pore networks from X-ray micro-CT images (Bultreys et al., 2018, 2020; Ellman et al., 2024; Raeini et al., 2017). The pore network extraction workflow begins by computing distance maps from void voxels to the nearest solid boundaries to identify pores and throats. Throats are segmented as constrictions between pores, while pores are further divided into half-throat corners. Corner conductivities are estimated using single-phase flow simulations.

Since natural rock pores typically exhibit irregular, angular geometries rather than idealised circular shapes, they promote the formation of corner wetting layers during fluid displacement, which significantly affect phase connectivity and trapping (Blunt et al., 2013; Hashemi et al., 2021a). To account for these corner wetting layers and snap-off events, the model assigns idealised cross-sectional shapes (circular, square, or triangular) based on geometric shape factors, which define the corner angles used to represent wetting layers in the network. In this approach, corner geometries are not extracted explicitly from the voxelised pore space but are instead approximated using idealised cross-sectional shapes derived from the calculated shape factor. For throats, the shape factor (G) is defined as,

$$G = \frac{R^2}{4A} \tag{1}$$

where R is the inscribed throat radius and A is the throat's cross-sectional area.

Pore shape factors are determined by averaging the shape factors of neighbouring throats, with weights assigned based on the shared cross-sectional area between the pore and each throat (Bultreys et al., 2018, 2020; Hashemi et al., 2021a; Raeini et al., 2017). The extracted network includes connectivity and geometric parameters, which are used as input for the flow simulations. The network statistics for both rock samples are provided in the Supplementary Section S1.

2.2.2. *Flow Simulation*

Flow simulations were performed using the open-source quasi-static pore-network flow solver ('pnflow', Imperial College, London) following the approach outlined in (Valvatne et al., 2004). The model assumes capillary-dominated, immiscible two-phase flow, where viscous pressure drops and interfacial mass transfer are neglected (Raeini et al., 2017). As such, all fluid interfaces are assumed static throughout the network except during discrete displacement events (Valvatne et al., 2004). This quasi-static approximation is consistent with the low capillary number (Ca $< 10^{-6}$) in the experiments, though we acknowledge it may not capture dynamic effects relevant to H_2 flow.

The model assumes immiscible flow and does not account for H_2 dissolution in water or water vapor in the gas phase. Fluid properties (Supplementary Section S2) were defined based on experimental conditions (50 °C, 100 bar) and held constant throughout the simulations. Contact angles were fixed at 30° for drainage (Hashemi et al., 2021b) and 54° for imbibition (Jangda et al., 2023), based on previous experimental measurements obtained with KI-containing brine, ensuring consistency with the wettability conditions of the experiments. While this simplification assumes spatially uniform and static contact angles, it provides a controlled basis for comparison. The choice of the contact angle (θ) values was further supported by a sensitivity analysis, described in the Supplementary Section S3, which shows that these θ values result in the closest match with experimental results. The interfacial tension is taken from published measurements for the H_2–water system under comparable conditions (Chow et al., 2018). The model does not explicitly account for potential changes in interfacial properties due to salinity or dissolved H_2, which could influence displacement behaviour under subsurface conditions.

To align the PNM simulations with the experimental conditions, the simulation was configured with the same flow direction as the experiments. Hydrogen was injected from the top of the sample during drainage, and water from the bottom during imbibition. The target saturation after drainage was adjusted to match experimental values (Bultreys et al., 2018; Øren et al., 2019). Without this constraint, the simulation will continue draining toward an unrealistically low brine saturation, approaching zero at infinitely high P_c. This outcome reflects the absence of a physical time scale in quasi-static models and the assumption that brine trapping is negligible due to the presence of continuous wetting layers along the corners of nearly all pores and throats (Bultreys et al., 2018). To account for end-effects and ensure consistency in post-processing, the simulation was run to a slightly higher H_2 saturation than measured, and the ends of the sample were cropped, as detailed in the results section. This allowed the central region of the simulation to better match experimental saturation values and enabled a more robust comparison of the associated pore-scale fluid distributions.

The model uses a quasi-static invasion-percolation algorithm, where fluid displacement is governed by entry P_c under the assumption that flow is slow enough for viscous forces to be negligible, and only capillary forces need to be considered (Øren et al., 2019; Ruspini et al., 2021; Wilkinson et al., 1983). At each step, the algorithm identifies candidate network elements for invasion and calculates their entry P_c, which are governed by the local pore geometry, wettability, and initial fluid configuration (Mayer et al., 1965; Øren et al., 2019; Piri et al., 2004; Ruspini et al., 2021; van Dijke et al., 2007; van Dijke et al., 2003).

Before drainage, all network elements are initially saturated with water. Drainage proceeds via piston-like displacement, where an element may only be filled with H_2 if an adjacent element already contains H_2. The element with the lowest entry P_c is invaded, and the global P_c is updated to that value if it is higher than the maximum P_c encountered so far (Bultreys et al., 2018, 2020; Lenormand et al., 1983). This sequence mimics the fluid displacement under capillary-dominated flow. The entry P_c values are calculated using the Young–Laplace equation (Blunt, 2016; Blunt et al., 2013) for circular cross-sections, and the Mayer–Stowe–Princen (MS-P) method (Mayer et al., 1965; Princen, 1969; Valvatne et al., 2004), which accounts for corner wetting and realistic interface curvature, for polygonal elements that constitute the majority of the pore space (Supplementary Section S1). The model incorporates wetting layers as such that H_2 occupies the centre of the network elements (pores and throats), and water remains in the corners. This means that trapping of water is relatively insignificant during drainage, as presence of water in the corners ensures global brine connectivity throughout the network (Valvatne et al., 2004).

Imbibition is more complex due to the variety of displacement mechanisms involved (Berg et al., 2016; Bultreys et al., 2020; Singh et al., 2022, 2019). The model accounts for three key processes during imbibition: piston-like displacement, cooperative pore-filling, and snap-off, the latter primarily occurring in throats. Piston-type displacement occurs when water invades a pore through a single connected throat, without altering the connectivity of the non-wetting phase. Cooperative pore filling occurs when a pore is invaded only after two or more neighbouring throats are filled with the wetting fluid. These events are labelled as I2, I3, and I4+ depending on the number of filled throats. They reflect a more complex displacement process in which the invading water meniscus simultaneously interacts with multiple neighbouring throats, allowing it to enter pores that would be inaccessible if only a single throat was available (Ellman et al., 2024; Singh et al., 2019). Snap-off occurs when wetting-phase layers in throat corners swell as P_c decreases and eventually coalesce. This displaces the non-wetting fluid from the centre of the throat, breaking the continuity of the non-wetting phase and promoting ganglia formation. Snap-off plays a significant role in phase trapping and connectivity alteration, particularly in water-wet systems (Singh et al., 2022, 2017).

At each stage of the invasion process, the algorithm identifies all accessible displacements, which are network elements where the wetting phase has a continuous entry path, and the non-wetting phase has an exit route, and ranks them by entry P_c. The threshold P_c for each displacement event is determined from the local pore or throat geometry and the imposed contact angle using capillary entry pressure relations implemented in the pnflow solver. The event with the highest P_c is executed first (Wilkinson et al., 1983), as the P_c is assumed to decrease slowly during imbibition (Ellman et al., 2024). The simulation maintains an initial water saturation and pressure in the pore-space, and as brine advances, H_2 clusters can become disconnected from the outlet. Snap-off events, particularly in narrow throats, accelerate this disconnection and contribute to the observed residual saturation. Once trapped, the P_c of these clusters becomes static, and they remain immobile for the remainder of the simulation (Bultreys et al., 2018; Valvatne et al., 2004). The model accounts for these displacement mechanisms to compute macroscopic quantities such as P_c–saturation relationships and relative permeabilities. However, we note that PNM predictions are non-unique due to the number of adjustable parameters and simplifying assumptions. This inherent limitation, along with the absence of viscous, gravitational, and interfacial kinetics, is discussed further in the manuscript.

The simulated flow results were post-processed to enable direct comparison with experimental observations. At each simulated displacement step, the model tracks the spatial distribution of H_2 and brine within the pore network. Using an in-house tool, the simulation outputs for each drainage and imbibition step were converted into a labelled image and mapped onto the geometry of the original micro-CT image of the dry rock using Avizo software. During this process, pores and throats identified in the PNM were assigned to the corresponding voxel regions of the segmented micro-CT image based on their spatial location and connectivity. The resulting labelled images therefore preserve the original micro-CT voxel resolution, enabling direct comparison between simulated and experimental phase distributions. The conversion process does not introduce artificial displacement of phases. However, minor uncertainties may arise from the initial pore-network extraction, where geometric simplifications of the pore space may lead to slight deviations in local invasion order. These effects do not significantly influence the overall phase occupancy or saturation distributions used for comparison with the experimental observations. Further details of this algorithm are provided in the Supplementary Section S4.

To quantify the H_2 saturation profile along the sample height, the number of voxels occupied by H_2 within each horizontal slice (5 μm thick) was computed using the volume fraction tool in Avizo. The H_2 saturation in each slice was then calculated as the ratio of H_2-filled voxels to the total number of pore voxels in that slice. This voxel-based saturation profile was then plotted against the sample height, providing a direct analogue to the experimental saturation measurement approach.

2.3. Comparison strategy

The goal of this systematic comparison is to evaluate whether the PNM accurately reproduces the H_2 saturation and spatial distribution observed in the experiments, and whether it predicts fluid occupancy in similar pores and throats of the rock. The comparison involves both quantitative and qualitative measures:

- **Fluid saturation profiles:** The vertical profile of H_2 saturation along the sample height.
- **Pore occupancy trends:** The distribution of H_2 across different pore sizes after drainage and imbibition.
- **Visual agreement:** Qualitative inspection of H_2 cluster locations and trapping within the pore network.

As the flow experiments were performed at constant flow rates and P_c was not measured during the experiments, the simulation and experimental results were compared for the drainage and imbibition stages based on the saturation levels observed in the experiments.

As shown in the following sections, the simulations closely replicate the experimental saturation and pore occupancy trends for the homogeneous Bentheimer sandstone, indicating that the model can represent capillary-dominated H_2 displacement in simple pore structures. For this rock type, additional simulations were conducted to explore the sensitivity of flow behaviour to contact angle variations and multiple drainage–imbibition cycles, which would be impractical to study experimentally due to time and resource constraints.

In contrast, the match for the heterogeneous layered Clashach sandstone is less accurate, particularly during imbibition. This reduced agreement may be attributed to the model's limited ability to capture fine-scale heterogeneities, spatial variability in wettability, and pore-body snap-off events, which are known to influence trapping and redistribution during imbibition (Ellman et al., 2024). Additionally, the quasi-static assumption may oversimplify the complex displacement dynamics that occur in more heterogeneous pore networks (Ruspini et al., 2021). The following section presents the results of these comparisons, highlighting the extent to which the PNM captures key features of H_2 displacement observed in the experiments across both rock types.

3. Results

Flow simulations were performed for both drainage and imbibition, first for the homogeneous Bentheimer sandstone and then for the heterogeneous Clashach sandstone. The results from the simulation were compared with experimental results (Jangda et al., 2023, 2024a).

3.1. Homogeneous Bentheimer sandstone – drainage

Visualisations of the H_2 phase after drainage from both the experiment and simulation are presented in Fig. 2A and Fig. 2B respectively. In both cases, H_2 primarily forms one large, connected cluster spanning the height of the sample, indicating that the model captures the dominant displacement and connectivity pattern. Although the saturation profile shows a reasonable comparison in Fig. 2D, there is some visual mismatch in the spatial distribution of H_2 in the pore space between the experimental and simulation results (Fig. 2A and 2B).

Certain regions that appear filled with H_2 in the experiment are not occupied in the simulation, and vice versa. While the mismatch in local H_2 placement introduces some uncertainty, it does not significantly affect the vertical saturation profile or large-scale connectivity. As a result, the model provides a reliable representation of drainage behaviour in this homogeneous rock.

The saturation profile plotted over the entire length of the rock sample (6.2 mm) shows the presence of end-effects in the simulation, particularly near the inlet. These arise from the model's boundary condition, where all throats connected to the inlet face are assumed to be in direct contact with a H_2 reservoir to initiate drainage. As shown in Fig. 2C, this leads to an artificially high H_2 saturation (∼ 70%), at the top of the sample, which corresponds to the injection face. To mitigate this artifact and enable a more accurate comparison, a cropped sub-volume of the rock was analysed, excluding 0.4 mm from the top and 0.8 mm from the bottom. As shown in Fig. 2D, the saturation profiles within this 5 mm central region align closely between experiment and simulation. The average post-drainage H_2 saturation in this region is 36.3% for both datasets.

Despite a close match in average saturation profiles between the experiment and simulation (Fig. 2D), notable differences are observed in the spatial distribution of H_2 in the pore space. Visual comparisons reveal that certain pores filled with H_2 in the experiment remain unfilled in the simulation, and vice versa (Fig. 3). This discrepancy arises from the inherently sensitive nature of quasi-static invasion-percolation processes. In the model, a pore can only be invaded if it has a filled neighbour, and the connecting throat radius is large enough to permit entry based on its entry P_c. Since multiple pores in the network have similar sizes and connectivity, slight differences in the invasion order can trigger different invasion paths. Once a pore is filled, its neighbours become accessible, potentially initiating a cascade of filling events that can propagate in multiple directions depending on local geometry and connectivity. This means that even small differences between the real and simulated pore structures can lead to markedly different displacement sequences (Ling et al., 2017). Although the exact spatial distribution of H_2 may differ, the model reproduces statistically similar saturation and pore occupancy trends. These statistical similarities can still provide meaningful insights for larger-scale predictive models, even if individual pore-level invasion events are not captured precisely.

The H_2 pore and throat occupancy analysis also shows a good statistical agreement between the experimental and simulation results (Fig. 2E and F). Specifically, an average pore radius of 35.6 μm for H_2-occupied pores is observed after drainage in the simulation model, closely aligning with the experimental value of 36.2 μm. Similarly, the average throat radius for H_2-occupied throats after drainage is 18 μm in the simulation, compared to 19 μm in the experimental results.

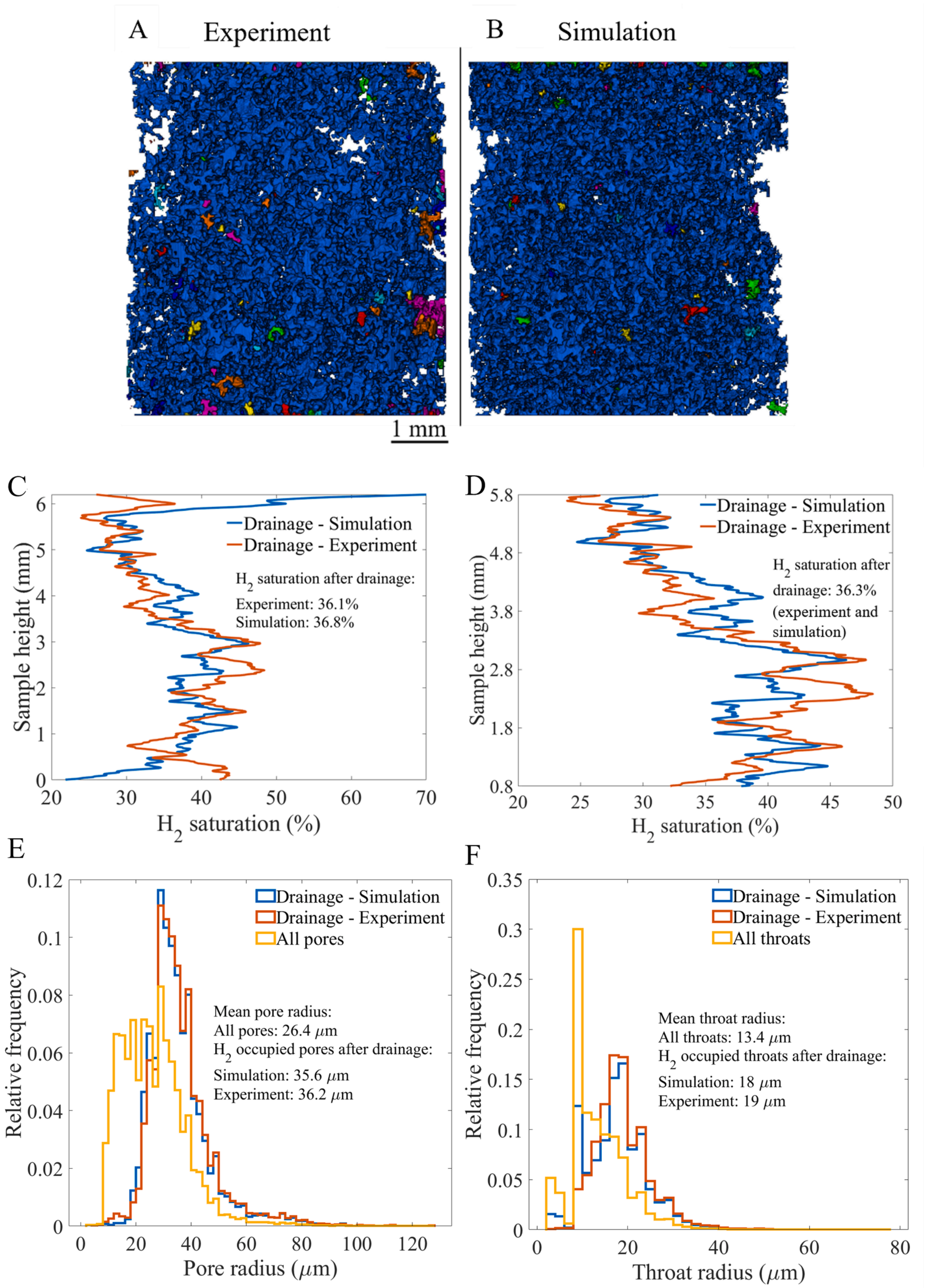

Fig. 2. Hydrogen distribution after drainage in the homogeneous Bentheimer sandstone from experiment and simulation. (A) 3D visualisation of H_2 clusters from the experiment and (B) the corresponding simulation. Each colour represents an individual disconnected H_2 cluster, with the large, connected cluster shown in blue. (C) Hydrogen saturation profiles over the full sample height, highlighting end effects in the simulation near the boundaries, and (D) saturation profiles over a cropped central region after removal of end effects. (E–F) Comparison of the radii (> 5 μm) of H_2-occupied pores (E) and throats (F) after drainage for the experiment and simulation. Distributions for all pores and throats are also shown. Histograms represent relative frequencies, with each distribution normalised by its own sample size.

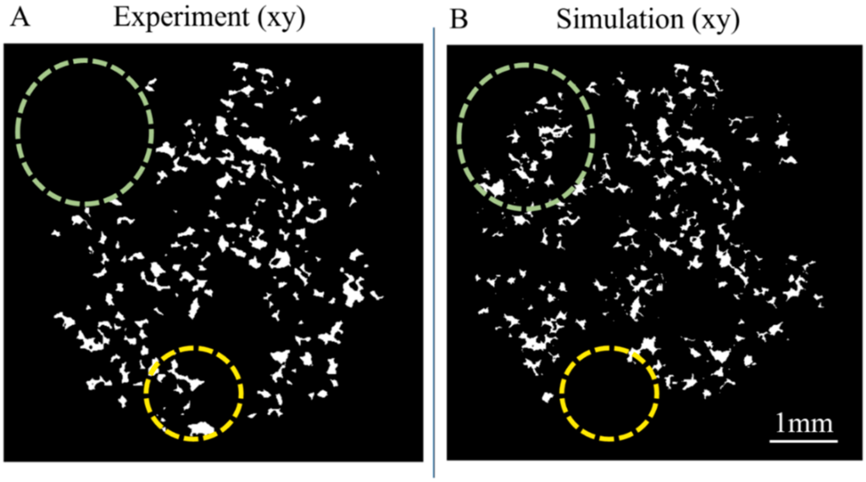

Fig. 3. 2D cross-sectional view (xy-plane) showing the distribution of the H_2 phase after drainage in the homogeneous Bentheimer sandstone. White regions indicate pores filled with H_2. Yellow dashed circles mark pores filled with H_2 in the experiment but not in the simulation. Green dashed circles indicate pores filled with H_2 in the simulation but not in the experiment.

3.2. Homogeneous Bentheimer sandstone – imbibition

In the next step, the simulation model was run for H_2 displacement by water (imbibition), aiming to reach a residual H_2 saturation. The imbibition simulation commenced from the state at which the drainage simulation was stopped. Visual representations of H_2 phases after imbibition are shown in Fig. 4A and Fig. 4B for both experimental and simulation cases. The visualisation shows that in both cases, the residual H_2 after imbibition is trapped as multiple disconnected ganglia, represented by different colours, compared to a large connected H_2 phase after drainage. This indicates that the model reproduces the general trapping behaviour seen in the experiment. However, visual differences can be observed in the ganglia distributions throughout the pore space between the experimental and simulation results. As contact angle strongly influences displacement dynamics and snap-off behaviour, a sensitivity analysis varying θ values was performed and is presented in the Supplementary Section S5.

The H_2 saturation profiles after imbibition (Fig. 4C and 4D) show close agreement between simulation and experiment in both spatial trend and residual saturation value. In the central cropped region, the model predicts a residual H_2 saturation of 25%, matching the experimental measurement. This agreement is noteworthy because the end-state saturation was not prescribed in the model for imbibition. The simulation began from the experimentally measured drainage saturation, which provided consistent initial conditions, and the resulting match in the final saturation reflects the model's ability to capture the overall displacement behaviour in a homogeneous rock.

The H_2 pore and throat occupancy analysis shows statistically consistent trends between the experiment and simulation in terms of pore occupancy. In both cases, H_2 preferentially resides in larger pores following imbibition, with the average radius of H_2-filled pores around 41 μm (Fig. 4E). However, there is a noticeable disparity in throat occupancy. The simulation predicts a higher number of throats occupied by H_2 compared to the experiment (Fig. 4F), with these throats also having a lower average throat radius. Despite this difference, the model demonstrates its capability to reasonably predict H_2-water fluid saturations and pore occupancies in a homogeneous rock sample, particularly when configured to match the observed drainage saturation during the experiment.

Although the model reproduces the overall saturation level and vertical distribution, noticeable differences are observed in the size and distribution of trapped H_2 ganglia as shown in Fig. 5. Both datasets show that a relatively small number of large ganglia dominate the total H_2 volume. However, the distributions of ganglia sizes differ significantly: the experimental dataset contains fewer ganglia overall (715 compared to 1630 in the simulation), with the majority concentrated in the intermediate size range (10^6–10^7 μm^3), whereas the simulation predicts a larger number of smaller ganglia predominantly within the ranges of 10^4–10^6 μm^3, which have minimal contribution to the overall H_2 saturation. Furthermore, the simulation results show that >50% of the total H_2 volume is attributed to the largest two ganglia (>10^9 μm^3), a feature not observed in the experimental data.

Such differences in ganglia size distribution can influence the predicted P_c and k_r relationships from the PNM. A higher proportion of smaller ganglia, with their larger surface-to-volume ratios, would be expected to increase the total H_2–brine interfacial area and curvature, potentially elevating the P_c (AlZaabi et al., 2025; Joekar-Niasar et al., 2012; Reeves et al., 1996). Conversely, the presence of very large H_2 ganglia can reduce wetting-phase connectivity, lowering brine k_r at a given saturation (Armstrong et al., 2016b; Rücker et al., 2015). This difference suggests that even in a homogeneous rock, the multiphase properties predicted by the PNM may not fully capture the underlying pore-scale processes and should be treated as approximate estimates rather than precise representations.

These outcomes are likely sensitive to key modelling assumptions, particularly the contact angle and its uniformity, as well as image resolution and geometric simplifications in network extraction. To investigate this, a contact angle sensitivity analysis is presented in the Supplementary Section S5 which shows that as θ increases (system becomes less water-wet), the number of snap-off events decrease, resulting in fewer but larger, more connected ganglia.

3.3. Heterogeneous Clashach sandstone – drainage

The simulation model was used to predict fluid displacements in the heterogeneous, layered Clashach sandstone, which presents a more complex pore structure than the Bentheimer sample. This sample contains a thin (~1.4 mm) low-permeability layer (Table 1) sandwiched between two thicker higher permeability layers.

Within the middle layer, a pathway of relatively larger throats (Supplementary Section S6) provides a preferential hydraulic connection between the top and bottom layers of the sample, enabling H_2 to bypass much of the low-permeability layer during drainage.

This structural heterogeneity significantly influences fluid distributions in the experiment, and while the model reproduces some qualitative features such as a single flow path within the low-permeability layer, it shows notable quantitative differences. Multiple factors may contribute to the model's limited accuracy in this case. First, the middle

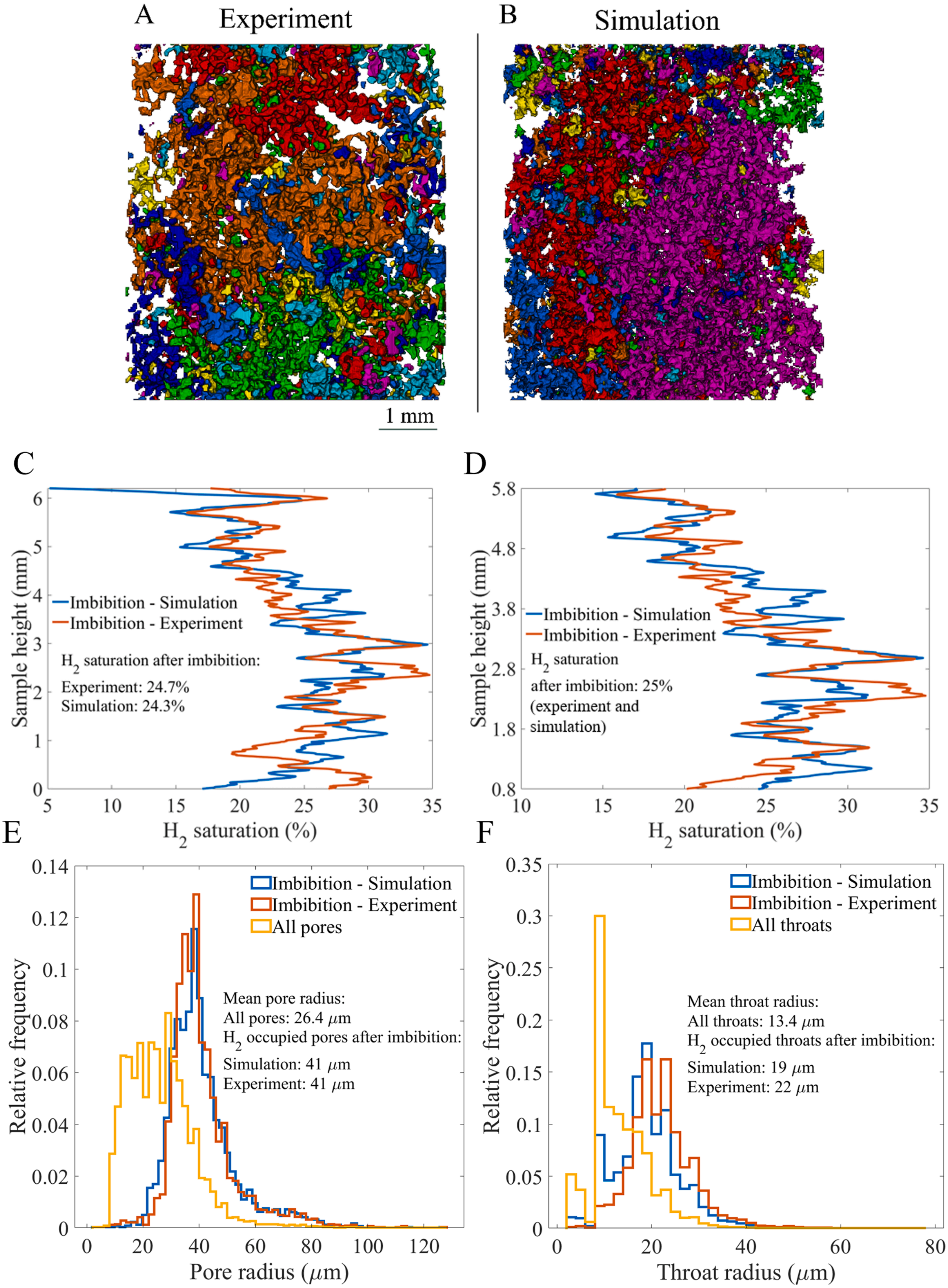

Fig. 4. Hydrogen distribution after imbibition in the homogeneous Bentheimer sandstone from experiment and simulation. (A) 3D visualisation of H_2 ganglia from the experiment and (B) the corresponding simulation. Colours represent individual disconnected H_2 ganglia formed after water injection. (C) Vertical H_2 saturation profiles over the full sample height, showing end effects in the simulation near the boundaries, and (D) saturation profiles over a cropped central region after removal of end effects. (E–F) Comparison of the radii (> 5 μm) of H_2-occupied pores (E) and throats (F) after imbibition for the experiment and simulation. Distributions for all pores and throats are also shown. Histograms represent relative frequencies, with each distribution normalised by its own sample size.

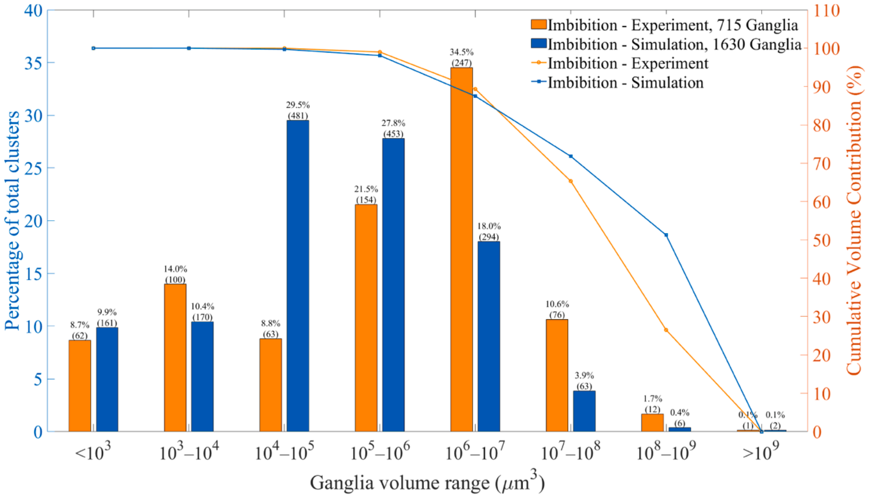

Fig. 5. Comparison of H_2 ganglia size distributions between experimental and simulation results after imbibition in homogeneous Bentheimer sandstone. Bars indicate the percentage (and number) of ganglia within defined volume ranges, while lines represent cumulative volume contributions of ganglia exceeding each threshold.

Table 1

Permeability of the different layers of the heterogeneous Clashach sample obtained using the simpleFoam solver in GeoChemFoam 5.0.

Parameter	Full sample	Bottom layer	Middle layer	Top layer
Sample height (mm)	0-8.44	0-3.67	3.67-5.11	5.11-8.44
Permeability (m^2)	1.0×10^{-12}	3.4×10^{-12}	5.1×10^{-13}	1.0×10^{-12}

layer may contain pores and throats that are difficult to resolve during image segmentation and network extraction, reducing geometric fidelity. Second, the difference in permeability and connectivity between the layers may trigger displacement phenomena that are inherently dynamic, for example, roof snap-off (Singh et al., 2017). These transient, viscous effects are not captured by the quasi-static, capillary-only model and could affect the timing and extent of H_2 invasion.

For the drainage simulation, model input parameters were set to align with experimental fluid saturations observed after drainage in the experiment. The visual representation of the predicted H_2 phase and the experimental observed H_2 after drainage are shown in Fig. 6A and 6B, highlighting the effects of the layered structure on the flow pattern.

As observed in the experiment, the model accurately predicts the flow of H_2 through a preferential pathway characterised by the lowest entry P_c in the middle layer. This implies that the model captures qualitative effects of the structural heterogeneity to an extent, aligning with the fluid flow behaviour observed in the experiment, despite quantitative disparities in fluid distributions evident in Fig. 6. At comparable fluid saturations, where the average H_2 saturation over the sample length closely matches between the experiment (36.6%) and the simulation (36.1%), the saturation profile displays discrepancies in the top and bottom layers. Specifically, the simulation predicts a lower average H_2 saturation in the top (37.6%) and a higher average H_2 saturation in the bottom layer (45.9%) compared to the experimental results of 60% and 27.7% respectively.

In the experiment, H_2 was injected from the top of the sample at a constant flow rate. As a result, H_2 accumulated in the top layer until the invasion pressure exceeded the entry pressure threshold of the lower permeability middle layer. This led to a noticeable pooling of H_2 above the middle layer. Once breakthrough occurred, H_2 preferentially followed a connected pathway of larger pores in the middle layer, bypassing much of the low-permeability zone and rapidly reaching the bottom layer. The simulation qualitatively captures the correct flow pathway through the middle layer but quantitatively underpredicts H_2 accumulation in the top layer and overpredicts saturation in the bottom layer. This discrepancy may stem from both model assumptions and imposed boundary conditions. In the PNM, P_c is assumed to equilibrate instantaneously across the entire domain. This differs from the dynamic pressure gradients present in the experiment, particularly across heterogeneous zones. While the PNM can capture pressure build-up from capillary constriction, it does not account for the pronounced, localised viscous pressure drop at the inlet of the lower permeability middle layer. The absence of this localised viscous effect in the model may lead to underestimation of H_2 accumulation above the middle layer before breakthrough.

In addition, the simulation prioritises invasion into larger pores based on capillary entry pressure rules. Since the bottom layer contains a higher proportion of larger pores, the model favours earlier filling of this region once access is established through the middle layer. In contrast, the experiment shows more gradual filling of smaller pores in the top layer prior to breakthrough. This is likely due to local pressure gradients and the time-dependent nature of interface movement, which are factors not captured by the quasi-static model.

The differences in the experimental observations and simulation predictions are further reflected in the H_2 pore occupancy analysis. In the top layer, the simulation predicts fewer H_2-filled pores (2051) compared to the experiment (2752), and with a slightly higher average pore radius (41 μm vs. 39 μm, Fig. 6E). This suggests that, in the experiment, increased local saturation enables H_2 to invade more small-radius pores prior to breakthrough. In the bottom layer, the simulation predicts more H_2-filled pores (2356) than the experiment (1129), with a slightly lower average pore radius (47 μm vs. 49 μm, Fig. 6F). This reflects the model's tendency to overfill larger, more connected pores in the absence of dynamic constraints. Furthermore, the simulation predicts fewer H_2-filled pores around the median pore radius in the top layer, and more in the same range in the bottom layer. This may suggest that the model slightly overestimates the ease of flow through the low-permeability middle layer, leading to earlier or more extensive invasion into the bottom layer than observed experimentally.

Altogether, the saturation profiles and pore occupancy comparisons illustrate that while the model can qualitatively predict fluid saturation and flow pathways, it lacks the ability to quantitatively simulate transient accumulation, pressure equilibration delays, and dynamic invasion phenomena. These limitations are particularly pronounced in heterogeneous systems where capillary entry pressures and pore accessibility vary significantly across the pore structure. The permeability contrast between the top, middle, and bottom layers creates localised pressure gradients that are not fully represented under the assumption of

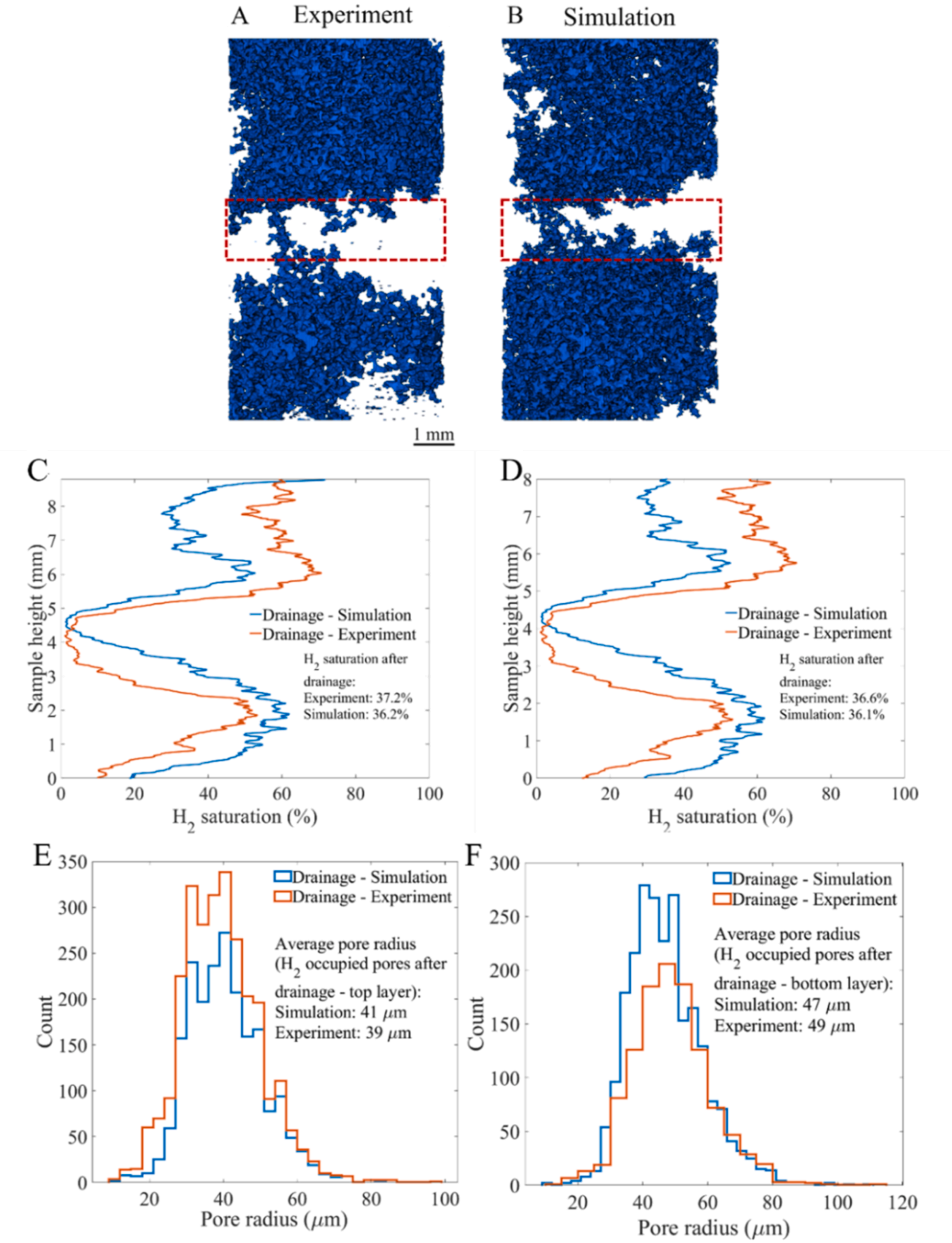

Fig. 6. Hydrogen distribution after drainage in the heterogeneous Clashach sandstone. (A) Experimental and (B) simulated 3D visualisations of the H_2 phase. The middle low-permeability layer is highlighted with red dashed boxes in both images; regions above and below this layer are referred to as the top and bottom layers, respectively (also see Fig. 1B). (C) Vertical H_2 saturation profiles along the full sample height show end-effects in the simulation near the inlet (top). (D) Saturation profiles for the cropped region, excluding the end-affected zones, enable more accurate comparison between simulation and experiment. The thickness of the bottom layer is 3.67 mm, while the thickness of the top layer is shortened from 3.3 mm to 2.9 mm. (E–F) Comparison of pore radii (>5 μm) of H_2-occupied pores after drainage for the top (E) and bottom (F) layers. The pore and throat size distributions for all the pores and throats of the different layers are provided in Supplementary Section S7.

instantaneous P_c equilibration. In the experiment, H_2 accumulates above the low-permeability middle layer until sufficient pressure builds to enable breakthrough. The quasi-static model, however, redistributes pressure globally and therefore underestimates this transient accumulation. In addition, the presence of a limited number of relatively large throats forming a preferential pathway through the middle layer (Supplementary Section S6) introduces abrupt connectivity transitions between layers. Once this pathway is accessed in the simulation, invasion into the bottom layer proceeds rapidly based solely on capillary entry pressures, favouring larger pores. In reality, viscous resistance and local pressure redistribution moderate this transition, which the PNM does not capture. These observations suggest that it is the combination of permeability contrast, sharp connectivity transitions, and the absence of dynamic pressure redistribution in the quasi-static PNM that limits the model accuracy.

Among the model inputs, contact angle plays a key role in controlling displacement mechanisms in quasi-static PNMs and can substantially influence predicted fluid distributions and saturations (Raeini et al., 2017, 2022), and varying the θ could help assess the robustness of simulation outcomes. Additionally, if the breakthrough pressure across the middle layer is available in the experimental data, it could provide a valuable reference point for validating the simulated entry pressures. However, such measurements are difficult to obtain in pore-scale core flow experiments.

3.4. Heterogeneous Clashach sandstone – imbibition

The imbibition simulation results deviate significantly from experimental observations. In the experiment, H_2 saturation decreased across all layers of the sample during imbibition, with residual H_2 remaining in

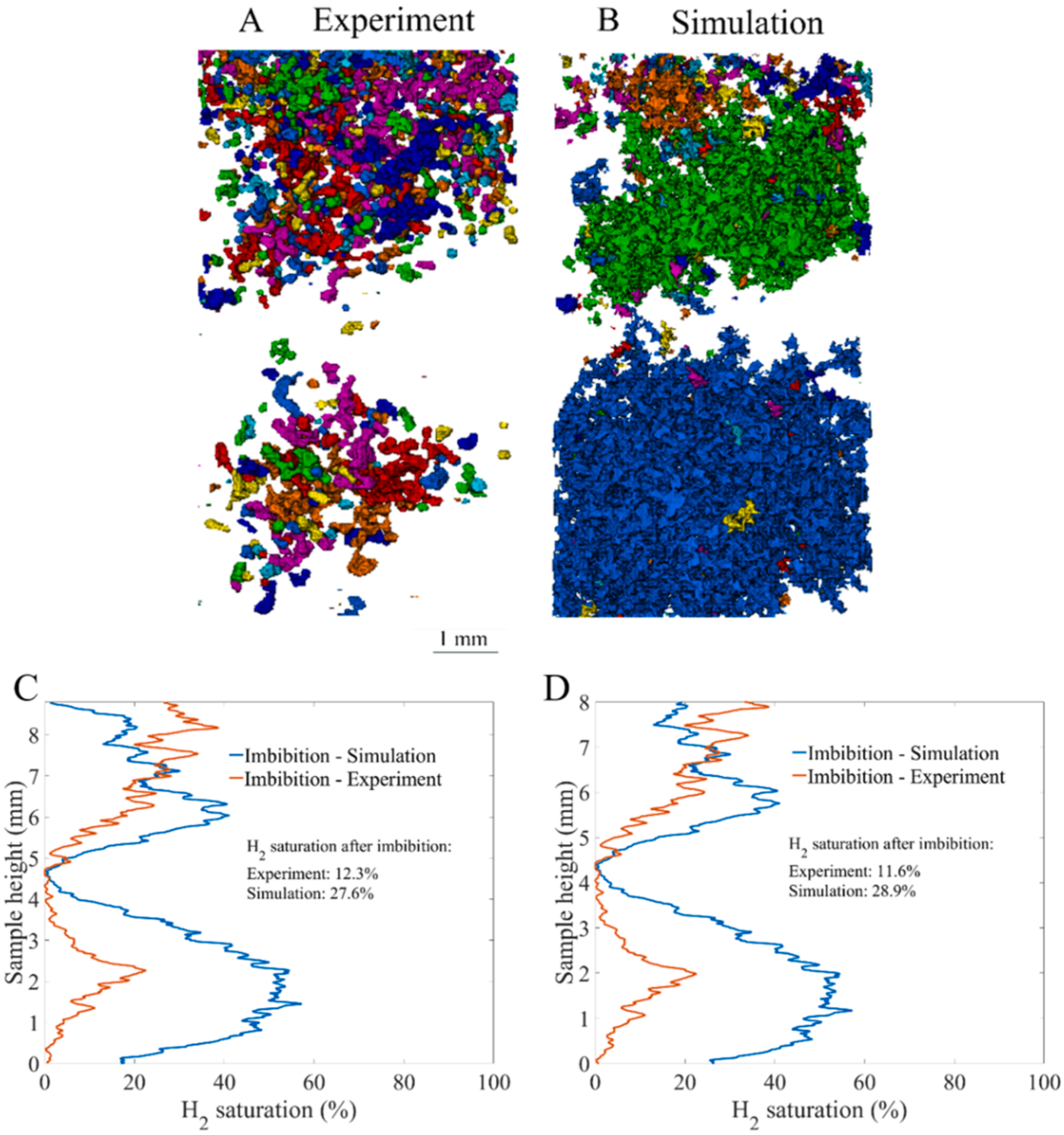

Fig. 7. Hydrogen phase distribution after imbibition in the heterogeneous Clashach sandstone. (A) Experimental result, showing multiple small, disconnected H_2 ganglia throughout the top and bottom layers. (B) Simulation result, with fewer but larger H_2 ganglia retained in both layers. Different colours represent individual disconnected H_2 ganglia. (C) Hydrogen saturation profiles after imbibition plotted along the full height of the rock sample for both simulation and experiment, showing simulation end-effects near the inlet. (D) Saturation profiles for a cropped region of the rock to reduce boundary artefacts and allow more accurate comparison.

the pore space as isolated ganglia (Fig. 7A). In contrast, the simulation predicts only a slight reduction in H_2 saturation, from 36.1% after drainage to 28.9% after imbibition. This discrepancy arises because, after predicting a snap-off event in the middle layer, the model seems to show no additional displacement or trapping of H_2 in the bottom layer. This behaviour likely reflects the quasi-static, capillary-dominated nature of the model, which excludes viscous mobilization and pressure-driven ganglia movement that may occur in the bottom layer during the experiment.

Although the simulated saturation profile diverges from the experimental data overall, it does capture some qualitative trends in the top layer (Fig. 7D), albeit with a poorer match than observed during drainage. However, in the bottom layer, the model predicts only a small reduction in H_2 saturation, from 45.9% to 40.4%, and retains a large, connected H_2 ganglion (Fig. 7B). This contrasts with the experimental observation of more extensive snap-off and ganglia breakup. While the model does indicate snap-off events in the middle layer, it does not reproduce the experimentally observed spatial distribution of trapped H_2, particularly in the bottom layer.

These discrepancies highlight well-documented limitations of quasi-static PNMs in modelling imbibition, especially in heterogeneous media (Bultreys et al., 2020; Ellman et al., 2024), where experimental observations likely provide a more accurate representation of the actual displacement and trapping processes. The model's predictive capacity is further constrained by mismatches carried forward from the drainage step, which directly influence the connectivity and configuration of H_2 at the start of imbibition (Bultreys et al., 2020; Ruspini et al., 2021). To accurately reproduce the experimental result, the model would need to capture not only the global saturation values, but also the specific sequence of trapping, snap-off, and disconnection events, as well as the local, non-uniform contact angles and their potential changes during fluid displacement. Given the complexity of the rock structure and the simplifications inherent to the PNM, achieving this level of spatial accuracy remains a challenge. Therefore, due to the discrepancies in fluid saturation and spatial distribution, a pore occupancy comparison between experimental and simulation results is not presented for the imbibition process.

3.5. *Morphological analysis of fluid phase distribution*

To further assess whether the PNM captures the geometrical characteristics of the H_2 phase beyond volumetric agreement, additional morphological descriptors were computed, including the Euler characteristic (χ) and interfacial area, using the *MatImage* toolbox (Legland, 2026). These analyses were performed for the homogeneous Bentheimer sandstone (drainage and imbibition) and the heterogeneous Clashach sandstone (drainage). While the overall H_2 saturation is closely matched between experiment and simulation for these cases, clear differences are observed in the pore-scale distribution of H_2 within the pore space.

For both rocks, the simulations consistently show more negative Euler characteristic values than the experiments, indicating a more connected H_2 phase. At the same time, the interfacial area predicted by the model is higher, suggesting that the H_2 phase is distributed in a more spatially extended manner within the pore space.

Overall, these results reinforce the observation that, although the PNM reproduces saturation and pore occupancy trends, it does not fully capture the connectivity and topology of the H_2 phase, highlighting a limitation of quasi-static PNMs. The computed Euler characteristic and interfacial area are summarised in Table 2.

Table 2
Comparison of Euler characteristic (χ) and interfacial area of H_2 for the experimental and simulated datasets.

Rock type	Process	Method	Euler characteristic (χ)	Interfacial area (mm^2)
Bentheimer	Drainage	Experiment	−1559	541
		Simulation	−7863	681
	Imbibition	Experiment	−395	320
		Simulation	−1928	445
Clashach	Drainage	Experiment	−1685	603
		Simulation	−4658	700

4. Discussion

4.1. *Scenario-based PNM predictions for homogeneous Bentheimer sandstone*

Given the agreement between the PNM simulation and experimental results for the homogeneous Bentheimer sandstone, the model was considered sufficiently validated for further analysis. In addition to successfully matching the H_2 saturation profiles, the model correctly predicts the preferential H_2 occupation of larger pores during drainage and the trapping of H_2 in larger pores after imbibition (Fig. 2 and Fig. 4). Based on this confidence, the model is used to explore additional scenarios, including the effects of θ variation and multiple drainage-imbibition cycles.

4.1.1. *Cyclic injection and production of H_2*

The PNM was further used to analyse the impact of multiple H_2 injection and withdrawal cycles on fluid saturation and distribution. As shown in Fig. 8, minimal saturation hysteresis was observed after the first injection–withdrawal cycle, with subsequent drainage and imbibition steps yielding nearly identical saturation profiles. These predictions are in agreement with previous results for a homogeneous Berea sandstone (Hashemi et al., 2021a), which similarly reports that saturation hysteresis stabilises after the initial cycle during cyclic H_2 injection and production.

However, despite the similarity in overall saturation profiles, differences in the spatial distribution of H_2 within the pore space are observed across the three drainage and three imbibition cycles, as shown in Supplementary Section S8. These differences may be attributed to the reconfiguration of fluid interfaces, changes in local connectivity, and pore-scale trapping pathways between cycles, even when the overall saturation is the same.

4.1.2. *Capillary pressure evolution across cycles*

The PNM simulations enable generation of P_c curves, providing insights beyond the experimentally obtained end-point fluid saturations. While these curves should not be interpreted as exact representations, given the limitations of image resolution, uncertain input parameters, and small sample domain, they are valuable for scenario testing. In this study, we generate P_c curves for multiple drainage–imbibition cycles as predicted by the PNM in the previous section. These curves help evaluate how P_c evolves across successive cycles and offer insights into saturation history effects.

The simulated P_c curves (Fig. 9) show that after each imbibition cycle, the P_c required to reach a given H_2 saturation during subsequent drainage cycles decreases. This trend reflects changes in the initial saturation state of the porous medium. During the first drainage cycle, the rock is fully water-saturated, and higher P_c values are required to overcome capillary entry thresholds. However, after imbibition, residual H_2 remains trapped, particularly in larger pores. When H_2 is reinjected during the second drainage, the presence of this trapped gas alters displacement pathways and facilitates earlier invasion, thereby reducing the P_c needed to achieve comparable saturation levels. Similar behaviour has been reported previously (Hashemi et al., 2021a) where the

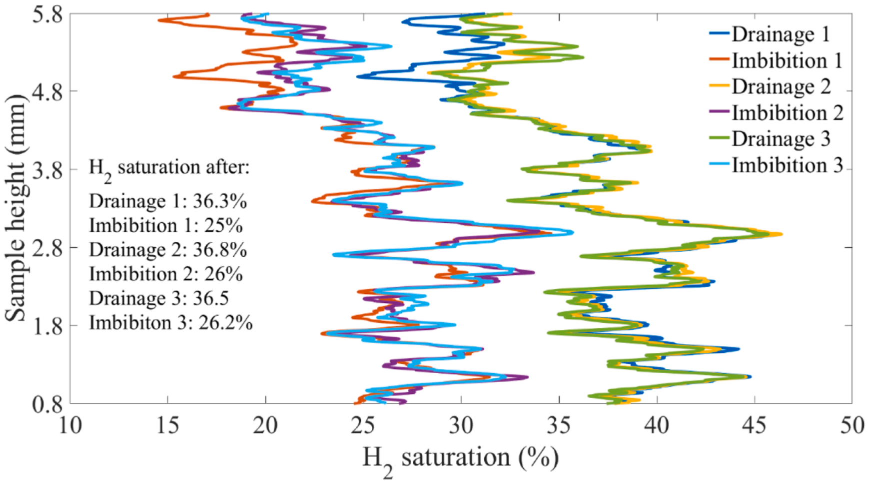

Fig. 8. Hydrogen saturation profiles after three drainage and imbibition cycles for the homogeneous Bentheimer sandstone plotted along the height of the rock sample.

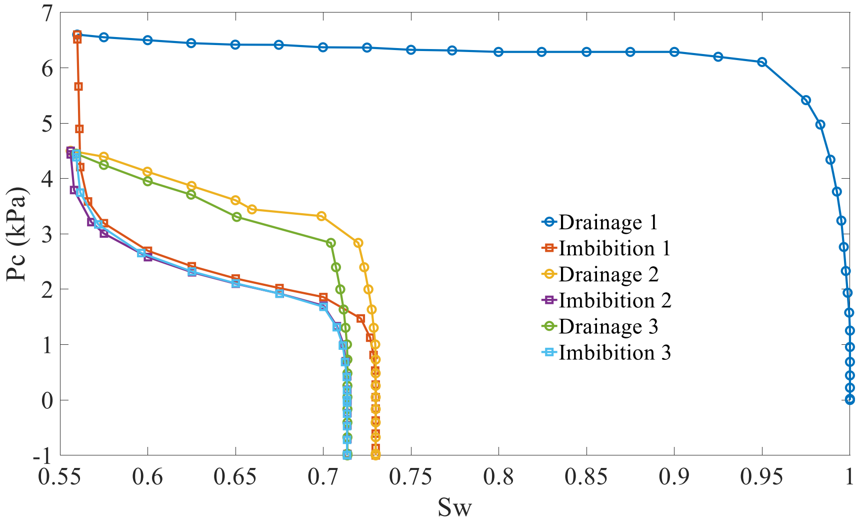

Fig. 9. Capillary pressure (P_c) vs water saturation (S_w) curves plotted for three drainage and imbibition cycles for the homogeneous Bentheimer sandstone as predicted by the PNM. The simulation model was adjusted to halt drainage at a H_2 saturation that matches the experimental H_2 saturation after drainage.

remaining H_2 phase after secondary imbibition led to lower P_c during subsequent drainage.

It should be noted that all drainage steps were terminated at the H_2 saturation corresponding to the experimentally observed value after the first drainage. As such, the curves do not represent full drainage to irreducible water saturation. If the simulations had continued to lower water saturations, the P_c curves might have converged more closely across cycles. However, due to persistent pore-scale trapping, complete convergence is unlikely.

The results demonstrate how PNM simulations can be used to explore the effects of cyclic injection on multiphase flow characteristics and gain insights into how P_c hysteresis influences subsequent flow behaviour. The overall shape and trend of the curves suggest that the system stabilises after the second cycle, with subsequent imbibition steps (e.g. imbibition 3 and potentially imbibition 4 onwards) converging toward a repeatable response. These curves are consistent with the similarity observed in the saturation profiles predicted by the PNM across multiple drainage–imbibition cycles (Fig. 8) and with earlier findings (Hashemi et al., 2021a), which also show that the hysteresis effect remains consistent after the first injection–production cycle.

4.1.3. Influence of wettability on fluid displacement and trapping

The PNM can also predict H_2 displacement under different wettability conditions, allowing investigation of how contact angle influences P_c and trapping mechanisms (Hashemi et al., 2021a). Wettability plays a critical role in controlling fluid displacement, ganglia trapping, and pressure thresholds required for fluid invasion in porous media (Krevor et al., 2023; Raeini et al., 2022; Wang et al., 2023b; Zhao et al., 2016).

For drainage, simulations were performed using four contact angle scenarios: uniform contact angles of 30° and 54°, and randomly distributed contact angles between 15°–45° and 10°–60°. As shown in Fig. 10A, higher contact angles result in lower capillary entry pressures. This relationship arises from the Young–Laplace equation, given by,

$$Pc = \frac{2\,\gamma\,\cos\theta}{r} \tag{2}$$

where Pc is the capillary entry pressure [Pa], γ is the interfacial tension [N.m^{-1}], θ is the contact angle [°], and r is the pore/throat radius [m].

Since $\cos(30^\circ) \approx 0.866$ and $\cos(54^\circ) \approx 0.588$, the entry pressure for 30° is 1.474 times greater than for 54°, assuming constant γ and r. An increase in θ leads to a reduction in capillary entry pressure, allowing H_2 to displace water more easily, indicative of a transition from strong to

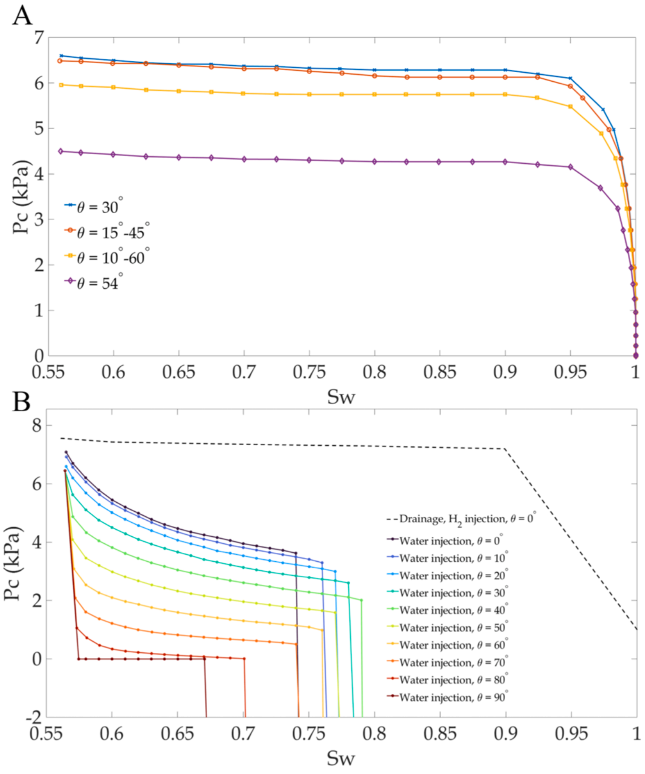

Fig. 10. Sensitivity analysis of (A) H_2 injection and (B) water injection in the Bentheimer sandstone under different contact angles, representing variation in wettability conditions. In (A) the H_2-injection curves correspond to a uniform contact angle of 30° and 54°, and a contact angle distribution of $15^\circ - 45^\circ$ and $10^\circ - 60^\circ$, while in (B) the H_2-injection curve corresponds to a contact angle of 0°, and the water-injection curves correspond to uniform contact angles between 0° and 90°.

moderate water-wet conditions. For drainage, changing θ to a different fixed value primarily scales the P_c curve, because the order of pore- and throat filling remains the same. By contrast, a distributed θ introduces variability in entry pressures across pores, altering the filling sequence and making the displacement less dependent on pore size.

For imbibition, a detailed sensitivity analysis was conducted for contact angles from 0° to 90°. All water injection simulations followed a drainage scenario with $\theta = 0^\circ$, terminated at the same saturation level. As shown in Fig. 10B, the imbibition P_c curves vary noticeably across the full range. Unlike drainage, changing θ alters the order of pore-scale filling events because imbibition involves multiple filling mechanisms, including piston-type displacement, cooperative pore-filling, and snap-off, each of which responds differently to the imposed θ. As a result, the nature of local displacement affects the size and connectivity of trapped H_2 ganglia.

In the lower θ cases, displacement begins at higher P_c and progresses more gradually, leading to relatively efficient H_2 removal. At higher θ values, particularly between 70° and 90°, displacement initiates at lower P_c and spans a narrower pressure range, which suggests increased capillary resistance and a stronger tendency for bypassing. The model also predicts that the lowest residual water saturation, and therefore the highest trapped H_2 saturation, occurs at $\theta = 90^\circ$. At this θ, trapping does not predominantly occur via snap-off, and the residual phase is instead dominated by fewer but larger ganglia. This aligns with the expectation that cooperative pore-body filling contributes more strongly at higher θ and that the overall trapping behaviour arises from the combined influence of several mechanisms rather than from snap-off alone (Spiteri et al., 2008).

The frequency of throat snap-off predicted by the model is highest for the intermediate θ range. In this interval, thin water layers are still present in pore corners but are less stable, creating conditions that promote frequent snap-off events (Spiteri et al., 2008). While the model predictions help illustrate qualitative trends, it is important to note that the simulations represent a capillary-dominated system and do not capture dynamic effects such as viscous coupling or time-dependent film motion. The statistical classifications are therefore intended for qualitative interpretation, and further experimental work will be needed to assess how closely these patterns match true invasion sequences during H_2 displacement in porous media.

The model also indicates clear shifts in the pore-filling process as θ increases. At lower θ, almost all pore-filling events occur through piston-type displacement, and no cooperative pore-body filling is observed. As θ increases, however, pore-body filling events (I2, I3, I4+) begin to appear and become substantially more frequent at $\theta = 80^\circ$–90°, as shown in Fig. 11A. In addition, a limited number of pore-scale snap-off events are observed at $\theta = 80^\circ$, while being largely absent at other contact angles. This suggests that this condition lies close to a transitional regime in which wetting layers can still form in sufficiently acute pore corners, consistent with the geometric criteria governing film stability, but remain unstable and collapse locally. Together, these trends suggests that the invading phase begins to reorganise the flow within pore bodies at high θ, selectively filling more accessible regions while leaving isolated volumes uninvaded. Such behaviour offers one explanation for the rise in trapping at high θ, even when throat snap-off is limited.

A similar pattern is observed in the throat filling process. At θ below 50°, piston-type filling accounts for most invasion events, indicating smooth advancement of the water-front across the network. Snap-off contributes a smaller fraction of the total events. As θ increases between 50° to 80°, piston-type filling becomes less frequent, accompanied by a rise in snap-off events. This pattern reverses at $\theta = 90^\circ$, where snap-off is absent but piston-type displacement increases sharply. The rise and fall of snap-off, coupled with the variation in piston-type events, suggests a redistribution of flow pathways as θ changes. These predictions are represented in Fig. 11B, which shows the number of piston and snap-off events for each θ.

These changes in fluid displacement behaviour are reflected in the post-imbibition water saturation, shown in Fig. 11B. Water saturation increases between $\theta = 0^\circ$ and 40°, consistent with relatively effective displacement and broad access of the invading phase to the pore network. Beyond this range, saturation declines, which indicates a growing tendency for H_2 to be bypassed and left behind as isolated ganglia. The reduction becomes most pronounced between $\theta = 70^\circ$ and 90°, suggesting that water advances through a more limited set of pathways, leaving significant portions of the pore space uninvaded.

The number of trapped H_2 elements and regions follow a similar pattern, where elements refer to the total number of individually trapped H_2 elements, and regions represent connected clusters of trapped H_2 (Fig. 11C). At lower θ, the number of disconnected clusters and the total trapped volume both decline between 0° and 30°, consistent with efficient H_2 mobilisation. As θ increases, the number of trapped clusters and the total trapped elements begin to rise, initially modestly and then more sharply beyond 60°. Between 70° and 90°, the number of trapped clusters increases markedly. Although the number of individual trapped elements decreases at $\theta = 90^\circ$, the clusters that remain tend to be larger, resulting in a higher overall trapped saturation. These observations suggest that trapping arises from the combined influence of piston-type invasion, snap-off and cooperative pore-body filling, each becoming more or less significant across the θ range (Spiteri et al., 2008).

Collectively, these results suggest that the model does not exhibit a simple monotonic relationship between θ and trapping. Instead, the displacement mechanisms reorganise progressively as θ changes. Piston-type displacement is dominant at low θ, snap-off is most active at intermediate θ and cooperative pore-body filling becomes increasingly important at high θ. The resulting trapping behaviour appears to emerge from the cumulative effects of these processes rather than being

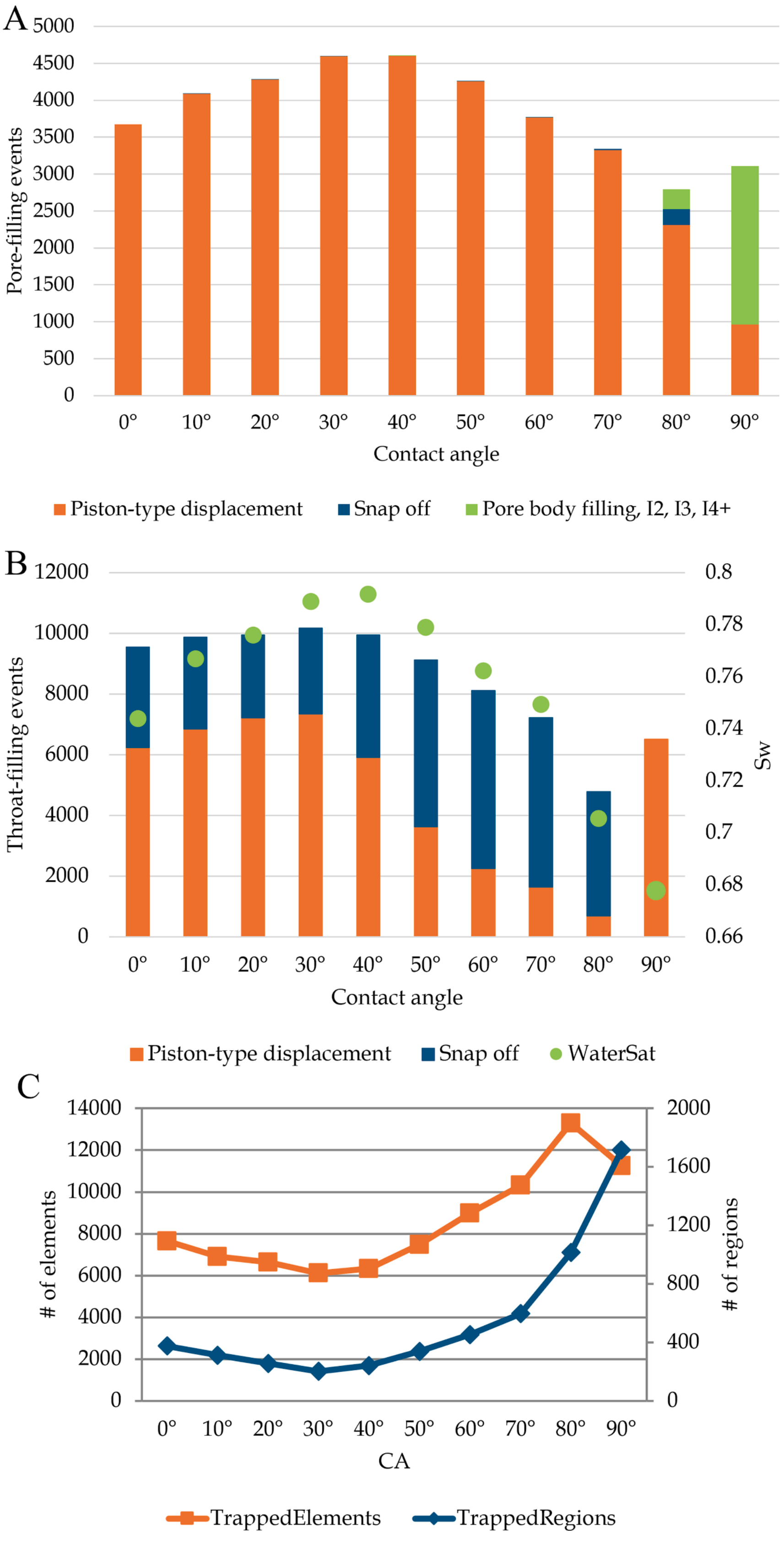

Fig. 11. Classification of (A) pore invasion mechanisms, (B) throat invasion mechanisms, and (C) trends in the number of trapped H_2 elements and trapped regions for each contact angle scenario during water injection (imbibition) in the homogeneous Bentheimer sandstone. In (B) the corresponding residual water saturation (WaterSat – S_w) is shown on the right-hand y-axis for each contact angle. In (C), at 90°, where residual water saturation is lowest and trapped H_2 saturation is highest, the number of trapped regions is greatest despite the number of trapped elements not being maximal, indicating that fewer but larger trapped ganglia dominate the residual phase.

controlled by any single mechanism acting alone.

In the present simulations, contact angles were assumed spatially uniform and temporally constant. In natural systems, however, wettability may vary spatially due to mineralogical heterogeneity (Iglauer et al., 2021) and temporally due to changing saturation history or microbial activities (Boon et al., 2024). Spatial wettability heterogeneity could alter local entry pressures and invasion sequences, leading to more irregular displacement pathways and potentially enhancing or suppressing snap-off in specific regions. Dynamic wettability effects during imbibition, including contact angle hysteresis, may further influence ganglion breakup and connectivity (Rücker et al., 2015). Imbibition involves multiple competing displacement mechanisms and is therefore likely more sensitive to such effects than drainage. Incorporating spatially variable or dynamic wettability into PNMs may therefore improve predictions of displacement and trapping behaviour.

Although PNMs do not provide exact quantitative predictions due to the absence of dynamic processes and fluid properties, they offer physically informed interpretations that help evaluate how wettability evolution may influence displacement and trapping in H_2 storage formations. These model-based insights, however, require experimental validation to confirm their applicability under realistic subsurface conditions.

4.2. Connection to previous PNM studies

The results from this study are evaluated in the context of previous studies that used similar modelling techniques for other fluid systems and rock types, including oil–water and CO_2–brine systems. Although a previous work (Hashemi et al., 2021a) used the same flow simulation model as in our study for H_2-brine systems, they limit their comparison to match k_r and P_c curves with literature data, without saturation, pore occupancy or visual analysis. Our work extends this by incorporating both qualitative and quantitative comparisons of fluid distributions, offering a more comprehensive evaluation of the PNM.

As presented earlier, the PNM results show good agreement with experimental data, particularly for the homogeneous water-wet system. This is consistent with earlier findings, where discrepancies of $<3\%$ during drainage and 7% during imbibition are reported for octane–brine systems (Øren et al., 2019), and a 75% pore occupancy match is achieved for CO_2–brine using the same PNM (Bultreys et al., 2018). Similarly, Yang et al. (Yang et al., 2017) use a dynamic PNM for oil–water systems and also report a 75% match during drainage. Their results suggest that even with the inclusion of viscous and capillary forces, achieving an exact pore-by-pore match remains challenging.

While exact pore-by-pore matching remains elusive, previous studies (Bultreys et al., 2018, 2020) suggest that statistical agreement in fluid occupancy and connectivity is sufficient for accurate prediction of upscaled properties. Discrepancies between experimental and simulated fluid distributions, especially at the pore-scale, do not necessarily translate into significant errors in macroscopic flow properties (Bultreys et al., 2020). Additionally, even repeat pore-scale experiments are not reproducible on a pore-by-pore basis (Ferrari et al., 2015; Ling et al., 2017). For example, in repeated drainage–imbibition experiments on Bentheimer sandstone, the standard deviation of the filling state was found to be up to 25% for the most variable pores, while the large-scale behaviour did not vary significantly (Bultreys et al., 2018). The filling discrepancy between the PNM simulation and experiments is therefore comparable to the difference between two repeat experiments that are macroscopically nearly indistinguishable. This implies that quasi-static PNMs may have practical utility to predict average properties, provided that the statistical characteristics of the fluid distributions are well captured. Our results support this view, as in the homogeneous system, the overall saturation profiles and connectivity patterns are well captured despite local discrepancies.

The observations in this work agree with earlier studies (Bultreys et al., 2018; Ellman et al., 2024; Øren et al., 2019) that imbibition remains more challenging to model accurately. Discrepancies in fluid distributions during imbibition are often attributed to the quasi-static assumption, which neglects dynamic effects such as ganglion dynamics and rapid fluid reconfigurations (Bultreys et al., 2020; Ellman et al., 2024). Our results also show mismatches in H_2 cluster sizes and connectivity during imbibition for the homogeneous rock, similar to the findings of Bultreys et al. (2018), who observed that the model predicted one large oil cluster with fewer smaller clusters compared to experiments. The lack of snap-off events in quasi-static models during imbibition, as noted by Ellman et al. (Ellman et al., 2024), is also observed in our simulations.

Contact angle sensitivity analysis across multiple studies (Ellman et al., 2024; Øren et al., 2019) and our own work confirms that accurate contact angle values improve model predictions. We found that using in-situ measured θ values from experiments led to the best match with experimental results, an observation also supported by recent studies (Ellman et al., 2024; Foroughi et al., 2025). Additionally, stopping the drainage simulation at the experimentally observed saturation, as implemented in this study, improves the basis for comparison during imbibition (Bultreys et al., 2018; Ruspini et al., 2021). Bultreys et al. (2020) further emphasised that providing the model with the experimental post-drainage fluid distribution, rather than the simulated one, enhances the accuracy of imbibition predictions.

Several avenues for improving the accuracy of PNMs emerge from this comparative analysis. Using a multiscale PNM (Ruspini et al., 2021) can enhance predictions in heterogeneous rocks. The lack of a good match in our heterogeneous system may be addressed by adopting this approach. The use of advanced cooperative pore-filling algorithms (Raeini et al., 2017; Ruspini et al., 2017) and improved network extraction methods (Øren et al., 2019; Zhan et al., 2024, 2022) can better capture complex displacement events, particularly during imbibition. Further benchmarking of PNM results against time-resolved experimental data (Bultreys et al., 2020; Ellman et al., 2024) could also improve the accuracy of model predictions. Additionally, a more detailed comparison of interfacial morphology using descriptors such as interfacial area, curvature, or topological measures could provide further insight into the geometric structure and connectivity of the fluid phases.

5. Conclusion

This study uses a quasi-static PNM, informed by pore-scale flow visualisation experiments, to evaluate H_2 flow and trapping behaviour in both homogeneous and heterogeneous sandstone rocks. The results show that while the PNM captures key displacement trends in a homogeneous rock, its predictive accuracy decreases in a more structurally heterogeneous rock, particularly during imbibition.

For the homogeneous Bentheimer sandstone, the PNM reproduces the H_2 saturation profiles and pore occupancy trends observed in experiments. Both drainage and imbibition simulations provide H_2 saturations that closely match the experimental values, with 36.3% after drainage and 25% after imbibition. The ability of the PNM to extend predictions to multiple flow cycles and varying wettability conditions demonstrates its usefulness as a computationally efficient tool for exploring scenario-based behaviour for UHS.

In contrast, the PNM simulations for the heterogeneous Clashach sandstone show marked deviations from the experimental results, especially during imbibition. The model overpredicts residual H_2 saturation (28.9% compared with 11.6% in the experiment), which would translate into an underestimate of recoverable H_2 from a layered reservoir. It also fails to reproduce key features such as spatial snap-off and fluid redistribution within the pore space. These mismatches are attributed to the limitations of a quasi-static PNM in heterogeneous rocks, as it does not fully capture the pore-scale mechanisms that influence fluid behaviour in the experiment.

These findings align with previous studies showing that PNMs generally perform better for drainage, where displacement processes are comparatively simpler, than for imbibition, which involves more complex fluid redistribution and ganglia trapping mechanisms (Ellman et al., 2024; Gostick et al., 2022; Helland et al., 2017). The results emphasise that a well-matched drainage simulation leads to a closer alignment of imbibition predictions, as observed for the homogeneous rock. Conversely, when drainage results deviate in the heterogeneous rock, imbibition predictions also show greater discrepancies. This mismatch highlights that the accuracy of imbibition predictions in the PNM is closely tied to how well the preceding drainage step is captured, as the initial saturation state significantly influences the subsequent displacement behaviour.

The results indicate that the predictive capability of the quasi-static PNM depends not only on the fluid displacement process but also on pore-structure characteristics. The model performs reliably in the homogeneous rock, which is characterised by relatively uniform pore and throat sizes and limited large-scale pressure redistribution effects. Under these conditions, the simplified displacement rules reproduce statistically consistent saturation profiles and pore occupancy trends. In contrast, the heterogeneous rock exhibits permeability contrasts and variations in pore and throat sizes, including the presence of a tight layer. The comparatively smaller pores and throats in this layer may be represented by only a few voxels due to imaging resolution limits, making them difficult to resolve accurately. This introduces uncertainty in the extracted pore network, which can contribute to discrepancies between the model predictions and experimental observations.

Quasi-static PNMs remain constrained by simplifying assumptions, including the omission of processes such as diffusion and dissolution, which can influence flow behaviour during subsurface multiphase flow. Therefore, PNMs are best viewed as tools for capturing statistical trends and dominant displacement mechanisms under capillary-dominated conditions, rather than as predictive models of detailed pore-scale fluid configurations. Nevertheless, their computational efficiency enables systematic scenario evaluation and sensitivity analysis, supporting mechanistic understanding and identifying processes that warrant further investigation.

Future improvements should focus on refining network extraction techniques to enhance the accuracy of PNM predictions, particularly in heterogeneous formations. Moreover, experimental evaluation of PNM predictions is particularly needed for heterogeneous and structurally complex rock types, such as carbonate rocks, where pore scale processes are more challenging to characterise and simulate. While homogeneous systems have been well assessed in this study, the applicability of PNMs for predicting multiphase flow behaviour in heterogeneous rocks remain to be fully assessed.

CRediT authorship contribution statement

Zaid Jangda: Writing – original draft, Visualization, Software, Methodology, Investigation, Formal analysis, Data curation, Conceptualization. **Tom Bultreys:** Writing – review & editing, Software, Methodology, Investigation, Formal analysis, Data curation. **Zeyun Jiang:** Writing – review & editing, Visualization, Software, Investigation, Data curation. **Sajjad Foroughi:** Writing – review & editing, Software, Investigation, Formal analysis, Data curation. **Hannah Menke:** Writing – review & editing, Methodology, Investigation, Data curation. **Andreas Busch:** Writing – review & editing, Supervision, Methodology, Conceptualization. **Sebastian Geiger:** Writing – review & editing, Supervision, Methodology, Funding acquisition, Conceptualization. **Kamaljit Singh:** Writing – review & editing, Supervision, Resources, Project administration, Methodology, Investigation, Funding acquisition, Formal analysis, Conceptualization.

Declaration of competing interest

The authors declare that they have no known competing financial interests or personal relationships that could have appeared to influence the work reported in this paper.

Acknowledgement

The authors are thankful to Energi Simulation for providing partial funding for this research and The Digital Imaging Hub at the Institute of GeoEnergy Engineering, Heriot-Watt University for assisted access to their X-ray Tomography Facility.

Supplementary materials

Supplementary material associated with this article can be found, in the online version, at doi:10.1016/j.ijmultiphaseflow.2026.105776.

Data availability

The experimental datasets used for comparison with the pore-network model are publicly available via figshare (DOI: 10.6084/m9.figshare.20260968.v1) and zenodo (DOI: 10.5281/zenodo.8375682). The pore-network modelling code is open source and available at https://github.com/ImperialCollegeLondon/pnflow.

References

Alaamri, J., Chandra, V., Addassi, M., Hoteit, H., 2023. Experimental and numerical investigation of spontaneous imbibition in multilayered porous systems. Energy Fuels 37 (16), 11694–11706. https://doi.org/10.1021/acs.energyfuels.3c01411.

Alpak, F.O., Berg, S., Zacharoudiou, I., 2018. Prediction of fluid topology and relative permeability in imbibition in sandstone rock by direct numerical simulation. Adv. Water. Resour. 122, 49–59. https://doi.org/10.1016/j.advwatres.2018.09.001.

AlZaabi, A., Alzahrani, H.M., Alhosani, A., Bijeljic, B., Blunt, M.J., 2025. Wettability, pore occupancy, connectivity and Ostwald ripening of nitrogen, carbon dioxide, and hydrogen in carbonate rocks: a comparative study. Int. J. Hydrogen. Energy 135, 596–608. https://doi.org/10.1016/j.ijhydene.2025.04.399.

Armstrong, R.T., McClure, J.E., Berrill, M.A., Rucker, M., Schluter, S., Berg, S., 2016a. Beyond Darcy's law: the role of phase topology and ganglion dynamics for two-fluid flow. Phys. Rev. E 94 (4–1), 043113. https://doi.org/10.1103/PhysRevE.94.043113.

Armstrong, R.T., McClure, J.E., Berrill, M.A., Rücker, M., Schlüter, S., Berg, S., 2016b. Beyond Darcy's law: the role of phase topology and ganglion dynamics for two-fluid flow. Phys. Rev. E 94 (4), 043113. https://doi.org/10.1103/PhysRevE.94.043113.

Bakke, S., Øren, P.-E., 1997. 3-D pore-scale modelling of sandstones and flow simulations in the pore networks. SPE J. 2 (02), 136–149. https://doi.org/10.2118/35479-pa.

Berg, S., Ott, H., Klapp, S.A., Schwing, A., Neiteler, R., Brussee, N., Makurat, A., Leu, L., Enzmann, F., Schwarz, J.-O., Kersten, M., Irvine, S., Stampanoni, M., 2013. Real-time 3D imaging of Haines jumps in porous media flow. Proc. Natl. Acad. Sci. USA 110 (10), 3755–3759. https://doi.org/10.1073/pnas.1221373110.

Berg, S., Rücker, M., Ott, H., Georgiadis, A., van der Linde, H., Enzmann, F., Kersten, M., Armstrong, R.T., de With, S., Becker, J., Wiegmann, A., 2016. Connected pathway relative permeability from pore-scale imaging of imbibition. Adv. Water. Resour. 90, 24–35. https://doi.org/10.1016/j.advwatres.2016.01.010.

Blunt, M.J., 2016. Multiphase Flow in Permeable Media. Cambridge University Press. https://doi.org/10.1017/9781316145098.

Blunt, M.J., 2022. Ostwald ripening and gravitational equilibrium: implications for long-term subsurface gas storage. Phys. Rev. E 106, 4. https://doi.org/10.1103/PhysRevE.106.045103.

Blunt, M.J., Bijeljic, B., Dong, H., Gharbi, O., Iglauer, S., Mostaghimi, P., Paluszny, A., Pentland, C., 2013. Pore-scale imaging and modelling. Adv. Water. Resour. 51, 197–216. https://doi.org/10.1016/j.advwatres.2012.03.003.

Bondino, I., Hamon, G., Kallel, W., Kac, D., 2013. Relative permeabilities from simulation in 3D rock models and equivalent pore networks: critical review and way forward. Petrophys. - The SPWLA J. 54 (06), 538–546.

Boon, M., Buntic, I., Ahmed, K., Dopffel, N., Peters, C., Hajibeygi, H., 2024. Microbial induced wettability alteration with implications for underground hydrogen storage. Sci. Rep. 14 (1), 8248. https://doi.org/10.1038/s41598-024-58951-6.

Bultreys, T., Lin, Q., Gao, Y., Raeini, A.Q., Alratrout, A., Bijeljic, B., Blunt, M.J., 2018. Validation of model predictions of pore-scale fluid distributions during two-phase flow. Phys. Rev. E 97, 053104. https://doi.org/10.1103/PhysRevE.97.053104.

Bultreys, T., Singh, K., Raeini, A.Q., Ruspini, L.C., Øren, P.E., Berg, S., Rücker, M., Bijeljic, B., Blunt, M.J., 2020. Verifying pore network models of imbibition in rocks using time-resolved synchrotron imaging. Water. Resour. Res. 56. https://doi.org/10.1029/2019WR026587.

Chow, Y. T. F., Maitland, G. C., .& Trusler, J. P. M. (2018). Interfacial tensions of ($H2O$ + $H2$) and ($H2O$ + $CO2$ + $H2$) systems at temperatures of (298–448) K and pressures up to 45 MPa. 475, 37–44. https://doi.org/10.1016/j.fluid.2018.07.022.

Dong, H., Blunt, M.J., 2009. Pore-network extraction from micro-computerized-tomography images. Phys. Rev. E 80 (3), 036307. https://doi.org/10.1103/PhysRevE.80.036307.

Ellman, S., Mascini, A., Bultreys, T., 2024. Validating mechanistic models of fluid displacement during imbibition. Adv. Water. Resour. 183, 104590. https://doi.org/10.1016/j.advwatres.2023.104590.

Ferrari, A., Jimenez-Martinez, J., Borgne, T.L., Méheust, Y., Lunati, I., 2015. Challenges in modeling unstable two-phase flow experiments in porous micromodels. Water. Resour. Res. 51 (3), 1381–1400. https://doi.org/10.1002/2014WR016384.

Foroughi, S., Shojaei, M.J., Lane, N., Rashid, B., Lakshtanov, D., Ning, Y., Zapata, Y., Bijeljic, B., Blunt, M.J., 2025. A framework for multiphase pore-scale modeling based on micro-CT imaging. Transp. Porous. Media 152 (3), 18. https://doi.org/10.1007/s11242-025-02156-6.

Goodarzi, S., Zhang, Y., Foroughi, S., Bijeljic, B., Blunt, M.J., 2024. Trapping, hysteresis and ostwald ripening in hydrogen storage: a pore-scale imaging study. Int. J. Hydrogen. Energy 56, 1139–1151. https://doi.org/10.1016/j.ijhydene.2023.12.029.

Gostick, J.T., Misaghian, N., Yang, J., Boek, E.S., 2022. Simulating volume-controlled invasion of a non-wetting fluid in volumetric images using basic image processing tools. Comput. Geosci. 158, 104978. https://doi.org/10.1016/j.cageo.2021.104978.

Hashemi, L., Blunt, M., Hajibeygi, H., 2021a. Pore-scale modelling and sensitivity analyses of hydrogen-brine multiphase flow in geological porous media. Sci. Rep. 11 (1), 8348. https://doi.org/10.1038/s41598-021-87490-7.

Hashemi, L., Glerum, W., Farajzadeh, R., Hajibeygi, H., 2021b. Contact angle measurement for hydrogen/brine/sandstone system using captive-bubble method relevant for underground hydrogen storage. Adv. Water. Resour. 154, 103964. https://doi.org/10.1016/j.advwatres.2021.103964.

Heinemann, N., Alcalde, J., Miocic, J.M., Hangx, S.J.T., Kallmeyer, J., Ostertag-Henning, C., Hassanpouryouzband, A., Thaysen, E.M., Strobel, G.J., Schmidt-Hattenberger, C., Edlmann, K., Wilkinson, M., Bentham, M., Stuart Haszeldine, R., Carbonell, R., Rudloff, A., 2021. Enabling large-scale hydrogen storage in porous media - the scientific challenges. Energy Environ. Sci. 14, 853–864. https://doi.org/10.1039/d0ee03536j.

Helland, J.O., Friis, H.A., Jettestuen, E., Skjæveland, S.M., 2017. Footprints of spontaneous fluid redistribution on capillary pressure in porous rock. Geophys. Res. Lett. 44 (10), 4933–4943. https://doi.org/10.1002/2017GL073442.

Iglauer, S., Ali, M., Keshavarz, A., & (2021). Hydrogen wettability of Sandstone Reservoirs: implications for Hydrogen geo-storage. 48, e2020GL090814. https://doi.org/10.1029/2020GL090814.

Jangda, Z., Menke, H., Busch, A., Geiger, S., Bultreys, T., Lewis, H., Singh, K., 2022. Pore-Scale Visualization of Hydrogen Storage in a Sandstone at Subsurface Pressure and Temperature Conditions: Trapping, Dissolution and Wettability. https://doi.org/10.6084/m9.figshare.20260968.v1.

Jangda, Z., Menke, H., Busch, A., Geiger, S., Bultreys, T., Lewis, H., Singh, K., 2023. Pore-scale visualization of hydrogen storage in a sandstone at subsurface pressure and temperature conditions: trapping, dissolution and wettability. J. Colloid. Interface Sci. 629, 316–325. https://doi.org/10.1016/j.jcis.2022.09.082.

Jangda, Z., Menke, H., Busch, A., Geiger, S., Bultreys, T., Singh, K., 2024a. Subsurface hydrogen storage controlled by small-scale rock heterogeneities. Int. J. Hydrogen. Energy 60, 1192–1202. https://doi.org/10.1016/j.ijhydene.2024.02.233.

Jangda, Z., Menke, H., Busch, A., Geiger, S., Bultreys, T., Singh, K., 2024b. X-ray microcomputed tomography (μCT) datasets of hydrogen (H_2) drainage and imbibition in a layered sandstone at reservoir pressure and temperature conditions. https://doi.org/10.5281/zenodo.8375682.

Joekar-Niasar, V., Hassanizadeh, S.M., 2012. Uniqueness of specific interfacial area–Capillary pressure–Saturation relationship under non-equilibrium conditions in two-phase porous Media flow. Transp. Porous. Media 94 (2), 465–486. https://doi.org/10.1007/s11242-012-9958-3.

Krevor, S., de Coninck, H., Gasda, S.E., Ghaleigh, N.S., de Gooyert, V., Hajibeygi, H., Juanes, R., Neufeld, J., Roberts, J.J., Swennenhuis, F., 2023. Subsurface carbon dioxide and hydrogen storage for a sustainable energy future. Nat. Rev. Earth Environ. 4 (2), 102–118. https://doi.org/10.1038/s43017-022-00376-8.

Legland, D., 2026. MatImage (Version 1.2.5). GitHub. https://github.com/mattools/matImage.

Lenormand, R., Zarcone, C., Sarr, A., 1983. Mechanisms of the displacement of one fluid by another in a network of capillary ducts. J. Fluid. Mech. 135, 337–353. https://doi.org/10.1017/S0022112083003110.

Lindquist, W.B., Lee, S.-M., Coker, D.A., Jones, K.W., Spanne, P., 1996. Medial axis analysis of void structure in three-dimensional tomographic images of porous media. J. Geophys. Res.: Solid Earth 101 (B4), 8297–8310. https://doi.org/10.1029/95JB03039.

Lindquist, W.B., Venkatarangan, A., 1999. Investigating 3D geometry of porous media from high resolution images. Phys. Chem. Earth, Part A: Solid Earth Geodesy 24 (7), 593–599. https://doi.org/10.1016/S1464-1895(99)00085-X.

Lindquist, W.B., Venkatarangan, A., Dunsmuir, J., Wong, T.-f., 2000. Pore and throat size distributions measured from synchrotron X-ray tomographic images of Fontainebleau sandstones. J. Geophys. Res.: Solid Earth 105 (B9), 21509–21527. https://doi.org/10.1029/2000JB900208.

Ling, B., Bao, J., Oostrom, M., Battiato, I., Tartakovsky, A.M., 2017. Modeling variability in porescale multiphase flow experiments. Adv. Water. Resour. 105, 29–38. https://doi.org/10.1016/j.advwatres.2017.04.005.

Liu, H., Kang, Q., Leonardi, C.R., Schmieschek, S., Narváez, A., Jones, B.D., Williams, J. R., Valocchi, A.J., Harting, J., 2016. Multiphase lattice Boltzmann simulations for porous media applications. Comput. Geosci. 20 (4), 777–805. https://doi.org/10.1007/s10596-015-9542-3.

Maes, J., Menke, H.P., 2021. GeoChemFoam: direct modelling of multiphase reactive transport in real pore geometries with equilibrium reactions. Transp. Porous. Media 139 (2), 271–299. https://doi.org/10.1007/s11242-021-01661-8.

Mascini, A., Cnudde, V., Bultreys, T., 2020. Event-based contact angle measurements inside porous media using time-resolved micro-computed tomography. J. Colloid. Interface Sci. 572, 354–363. https://doi.org/10.1016/j.jcis.2020.03.099.

Mayer, R.P., Stowe, R.A., 1965. Mercury porosimetry—Breakthrough pressure for penetration between packed spheres. J. Colloid. Sci. 20 (8), 893–911. https://doi.org/10.1016/0095-8522(65)90061-9.

Miocic, J.M., Alcalde, J., Heinemann, N., Marzan, I., Hangx, S., 2022. Toward energy-independence and net-zero: the inevitability of subsurface storage in Europe. ACS. Energy Lett. 7 (8), 2486–2489. https://doi.org/10.1021/acsenergylett.2c01303.

Muhammed, N.S., Haq, B., Al Shehri, D., Al-Ahmed, A., Rahman, M.M., Zaman, E., 2022. A review on underground hydrogen storage: insight into geological sites, influencing factors and future outlook. Energy Reports 8, 461–499. https://doi.org/10.1016/j.egyr.2021.12.002.

Øren, P.E., Bakke, S., Arntzen, O.J., 1998. Extending predictive capabilities to network models. SPE J. 3 (04), 324–336. https://doi.org/10.2118/52052-PA.

Øren, P.E., Ruspini, L.C., Saadatfar, M., Sok, R.M., Knackstedt, M., Herring, A., 2019. In-situ pore-scale imaging and image-based modelling of capillary trapping for geological storage of CO_2. Int. J. Greenh. Gas Control 87, 34–43. https://doi.org/10.1016/j.ijggc.2019.04.017.

Øren, P.-E., Bakke, S., 2003. Reconstruction of Berea sandstone and pore-scale modelling of wettability effects. J. Petrol. Sci. Eng. 39 (3), 177–199. https://doi.org/10.1016/S0920-4105(03)00062-7.

Patsoukis Dimou, A., Menke, H.P., Maes, J., 2022. Benchmarking the viability of 3D printed micromodels for single phase flow using particle image velocimetry and direct numerical simulations. Transp. Porous. Media 141 (2), 279–294. https://doi.org/10.1007/s11242-021-01718-8.

Petrovskyy, D., van Dijke, M.I.J., Jiang, Z., Geiger, S., 2021. Phase connectivity in pore-network models for capillary-driven flow. Adv. Water. Resour. 147, 103776. https://doi.org/10.1016/j.advwatres.2020.103776.

Piri, M., Blunt, M.J., 2004. Three-phase threshold capillary pressures in noncircular capillary tubes with different wettabilities including contact angle hysteresis. Phys. Rev. E 70 (6), 061603. https://doi.org/10.1103/PhysRevE.70.061603.

Princen, H.M., 1969. Capillary phenomena in assemblies of parallel cylinders: I. Capillary rise between two cylinders. J. Colloid. Interface Sci. 30 (1), 69–75. https://doi.org/10.1016/0021-9797(69)90379-8.

Raeini, A.Q., Bijeljic, B., Blunt, M.J., 2017. Generalized network modeling: network extraction as a coarse-scale discretization of the void space of porous media. Phys. Rev. e 96 (1–1), 013312. https://doi.org/10.1103/PhysRevE.96.013312.

Raeini, A.Q., Blunt, M.J., Bijeljic, B., 2014. Direct simulations of two-phase flow on micro-CT images of porous media and upscaling of pore-scale forces. Adv. Water. Resour. 74, 116–126. https://doi.org/10.1016/j.advwatres.2014.08.012.

Raeini, A.Q., Giudici, L.M., Blunt, M.J., Bijeljic, B., 2022. Generalized network modelling of two-phase flow in a water-wet and mixed-wet reservoir sandstone: uncertainty and validation with experimental data. Adv. Water. Resour. 164, 104194. https://doi.org/10.1016/j.advwatres.2022.104194.

Ramstad, T., Idowu, N., Nardi, C., Øren, P.-E., 2012. Relative permeability calculations from two-phase flow simulations directly on digital images of porous rocks. Transp. Porous. Media 94 (2), 487–504. https://doi.org/10.1007/s11242-011-9877-8.

Reeves, P.C., Celia, M.A., 1996. A functional relationship between capillary pressure, saturation, and interfacial area as revealed by a pore-scale network model. Water. Resour. Res. 32 (8), 2345–2358. https://doi.org/10.1029/96WR01105.

Rücker, M., Berg, S., Armstrong, R.T., Georgiadis, A., Ott, H., Schwing, A., Neiteler, R., Brussee, N., Makurat, A., Leu, L., Wolf, M., Khan, F., Enzmann, F., Kersten, M., 2015. From connected pathway flow to ganglion dynamics. Geophys. Res. Lett. 42 (10), 3888–3894. https://doi.org/10.1002/2015GL064007.

Ruspini, L.C., Farokhpoor, R., Øren, P.E., 2017. Pore-scale modeling of capillary trapping in water-wet porous media: a new cooperative pore-body filling model. Adv. Water. Resour. 108, 1–14. https://doi.org/10.1016/j.advwatres.2017.07.008.

Ruspini, L.C., Øren, P.E., Berg, S., Masalmeh, S., Bultreys, T., Taberner, C., Sorop, T., Marcelis, F., Appel, M., Freeman, J., Wilson, O.B., 2021. Multiscale digital rock analysis for Complex rocks. Transp. Porous. Media 139 (2), 301–325. https://doi.org/10.1007/s11242-021-01667-2.

Ryazanov, A.V., van Dijke, M.I.J., Sorbie, K.S., 2009. Two-phase pore-network modelling: existence of oil layers during water invasion. Transp. Porous. Media 80 (1), 79–99. https://doi.org/10.1007/s11242-009-9345-x.

Schlüter, S., Berg, S., Li, T., Vogel, H.-J., Wildenschild, D., 2017. Time scales of relaxation dynamics during transient conditions in two-phase flow. Water. Resour. Res. 53 (6), 4709–4724. https://doi.org/10.1002/2016WR019815.

Silin, D., Patzek, T., 2006. Pore space morphology analysis using maximal inscribed spheres. Phys. A: Stat. Mech. Appl. 371 (2), 336–360. https://doi.org/10.1016/j.physa.2006.04.048.

Singh, K., Bultreys, T., Raeini, A.Q., Shams, M., Blunt, M.J., 2022. New type of pore-snap-off and displacement correlations in imbibition. J. Colloid. Interface Sci. 609, 384–392. https://doi.org/10.1016/J.JCIS.2021.11.109.

Singh, K., Jung, M., Brinkmann, M., Seemann, R., 2019. Capillary-dominated fluid displacement in porous Media. Annu Rev. Fluid. Mech. 51, 429–449. https://doi.org/10.1146/annurev-fluid-010518-040342.

Singh, K., Menke, H., Andrew, M., Lin, Q., Rau, C., Blunt, M.J., Bijeljic, B., 2017. Dynamics of snap-off and pore-filling events during two-phase fluid flow in permeable media. Sci. Rep. 7. https://doi.org/10.1038/s41598-017-05204-4.

Sorbie, K., Skauge, A., 2012. Can network modeling predict two-phase flow functions? Petrophysics 53, 401–409.

Spiteri, E.J., Juanes, R., Blunt, M.J., Orr, F.M., 2008. A new model of trapping and relative permeability hysteresis for all wettability characteristics. SPE J. 13 (03), 277–288. https://doi.org/10.2118/96448-pa.

Tarkowski, R., 2019. Underground hydrogen storage: characteristics and prospects. Renew. Sustain. Energy Rev. 105, 86–94. https://doi.org/10.1016/j.rser.2019.01.051.

Thaysen, E.M., Butler, I.B., Hassanpouryouzband, A., Freitas, D., Alvarez-Borges, F., Krevor, S., Heinemann, N., Atwood, R., Edlmann, K., 2023. Pore-scale imaging of hydrogen displacement and trapping in porous media. Int. J. Hydrogen. Energy 48 (8), 3091–3106. https://doi.org/10.1016/j.ijhydene.2022.10.153.

Thaysen, E.M., Butler, I.B., Hassanpouryouzband, A., Spurin, C., Freitas, D., Rizzo, R., Alvarez-Borges, F., Atwood, R., Edlmann, K., 2025. Time-resolved 2D and 3D imaging of hydrogen and brine displacement processes in porous Clashach sandstone. J. Colloid. Interface Sci. 694, 137704. https://doi.org/10.1016/j.jcis.2025.137704.

Valvatne, P.H., Blunt, M.J., 2004. Predictive pore-scale modeling of two-phase flow in mixed wet media. Water. Resour. Res. 40, 7. https://doi.org/10.1029/2003WR002627.

van Dijke, M.I.J., Sorbie, K.S., 2003. Three-phase capillary entry conditions in pores of noncircular cross-section. J. Colloid. Interface Sci. 260 (2), 385–397. https://doi.org/10.1016/S0021-9797(02)00228-X.

van Dijke, M.I.J., Sorbie, K.S., 2007. Consistency of three-phase capillary entry pressures and pore phase occupancies. Adv. Water. Resour. 30 (2), 182–198. https://doi.org/10.1016/j.advwatres.2005.03.024.

Wang, J., Yang, Y., Cai, S., Yao, J., Xie, Q., 2023a. Pore-scale modelling on hydrogen transport in porous media: implications for hydrogen storage in saline aquifers. Int. J. Hydrogen. Energy 48 (37), 13922–13933. https://doi.org/10.1016/j.ijhydene.2022.11.299.

Wang, Y.D., Chung, T., Rabbani, A., Armstrong, R.T., Mostaghimi, P., 2021. Fast direct flow simulation in porous media by coupling with pore network and Laplace models. Adv. Water. Resour. 150, 103883. https://doi.org/10.1016/j.advwatres.2021.103883.

Wang, Y., Chakrapani, T.H., Wen, Z., Hajibeygi, H., 2024. Pore-scale simulation of H_2-brine system relevant for underground hydrogen storage: a lattice Boltzmann investigation. Adv. Water. Resour. 190, 104756. https://doi.org/10.1016/j.advwatres.2024.104756.

Wang, Z., Pereira, J.-M., Sauret, E., Gan, Y., 2023b. Wettability impacts residual trapping of immiscible fluids during cyclic injection. J. Fluid. Mech. 961. https://doi.org/10.1017/jfm.2023.222.

Wildenschild, D., Sheppard, A.P., 2013. X-ray imaging and analysis techniques for quantifying pore-scale structure and processes in subsurface porous medium systems. Adv. Water. Resour. 51, 217–246. https://doi.org/10.1016/j.advwatres.2012.07.018.

Wilkinson, D., Willemsen, J.F., 1983. Invasion percolation: a new form of percolation theory. J. Phys. A Math. Gen. 16 (14), 3365–3376. https://doi.org/10.1088/0305-4470/16/14/028.

Yang, J., Bondino, I., Regaieg, M., Moncorgé, A., 2017. Pore to pore validation of pore network modelling against micromodel experiment results. Comput. Geosci. 21 (5–6), 849–862. https://doi.org/10.1007/s10596-017-9630-7.

Zhan, N., Wang, Y., Lu, X., Wu, R., Kharaghani, A., 2024. Pore-corner networks unveiled: extraction and interactions in porous media. Phys. Rev. Fluids. 9 (1), 014303. https://doi.org/10.1103/PhysRevFluids.9.014303.

Zhan, N., Wu, R., Tsotsas, E., Kharaghani, A., 2022. Proposal for extraction of pore networks with pores of high aspect ratios. Phys. Rev. Fluids. 7 (1), 014304. https://doi.org/10.1103/PhysRevFluids.7.014304.

Zhang, Y., Bijeljic, B., Gao, Y., Goodarzi, S., Foroughi, S., Blunt, M.J., 2023. Pore-scale observations of hydrogen trapping and migration in porous rock: demonstrating the effect of Ostwald ripening. Geophys. Res. Lett. 50, 7. https://doi.org/10.1029/2022gl102383.

Zhao, B., MacMinn, C.W., Juanes, R., 2016. Wettability control on multiphase flow in patterned microfluidics. Proc. Natl. Acad. Sci. USA 113 (37), 10251–10256. https://doi.org/10.1073/pnas.1603387113.

Zhao, B., MacMinn, C.W., Primkulov, B.K., Chen, Y., Valocchi, A.J., Zhao, J., Kang, Q., Bruning, K., McClure, J.E., Miller, C.T., Fakhari, A., Bolster, D., Hiller, T., Brinkmann, M., Cueto-Felgueroso, L., Cogswell, D.A., Verma, R., Prodanović, M., Maes, J., Juanes, R., 2019. Comprehensive comparison of pore-scale models for multiphase flow in porous media. Proc. Natl. Acad. Sci. USA 116 (28), 13799–13806. https://doi.org/10.1073/pnas.1901619116.

Zivar, D., Kumar, S., Foroozesh, J., 2021. Underground hydrogen storage: a comprehensive review. Int. J. Hydrogen. Energy 46 (45), 23436–23462. https://doi.org/10.1016/j.ijhydene.2020.08.138.